A Theoretical Model of Ultrasonic NDT: Signals from Facetted Cracks

from a CEGB Report of 1987

John Coffey, Cheshire, UK.

2025

Introduction

This document is a verbatim transcription for the CEGB report written by the author in 1987 describing my 'triangular tile' model of rough, facetted surfaces and the scattering of ultrasonic pulses from them. It models ultrasonic non-destructive testing (NDT), and is realistic and comprehensive in that it includes the pulse and beam shape from the ultrasonic probe, the scanning of the probe over the component's surface, the scattering of the pulse from a facetted crack, and the rectified received signal in the usual back-scattered 'pulse-echo' configuration. Included in this is a model of the crack face, represented as a triangular mesh.

To explain the context, the author worked in research and development for the Central Electricity Generating Board, the publicly owned company which then owned and operated all the electricity power stations in England and Wales. I worked within a section called the Non-Destructive Testing Applications Centre which had responsibility for improving NDT techniques for power station plant – coal and oil fired, hydro-electric and nuclear. In the mid 1980s the CEGB, chaired by Lord Walter Marshall, was eager to introduce the pressured water reactor (PWR) into Britain, rather than build more CO_2-cooled nuclear power stations. Nuclear power generation was controversial in the UK as in many other countries, especially after the Chernobyl disaster of April 1986. Some leading academics were sceptical as to whether the PWR would be safe, and particularly wanted assurance that failure of the reactor pressure vessel and associated pipework would be 'incredible'[1]. Much stress and materials analysis was performed on the mechanical stability of the pressure vessel under various operating and shock conditions, and this was matched by the design of searching ultrasonic techniques for detecting and assessing any defects which might be present, whether they arose in manufacture or during service.

The most significant defects are cracks or crack-line planes such as lack of fusion at the side walls of welds, where surfaces have separated and created a sharp edge around the defect which concentrates stress. Ultrasonics was still being developed at the time as the most effective technique to detect cracks and measure their position, size and orientation. A

[1] The word 'incredible' was taken literally to mean 'not possible to be believed'.

variety of approaches were taken to prove the effectiveness of ultrasonics, including full scale demonstration trials on blocks of welded steel containing deliberately implanted cracks-like defects. These were complemented by theoretical analysis of the ultrasonic inspection process and in particular the scattering of ultrasonic waves from cracks. Since in principle cracks can be smooth and flat, or irregular and facetted, both types were examined. The 'triangular tile' model described in this report was created by the author to deal with facetted cracks. It was the first comprehensive model of the whole inspection process, allowing the simulation of ultrasonics signals received for a wide range of postulated hypothetical cracks. As the report describes, the team led by the author also constructed a measuring machine for scanning the height variations of cracks on a fine scale, to obtain quantitative data on the morphology of some types of crack. I expect that the subject have been much developed since 1987, though I changed career shortly after this report was written.

I assume that the reader is familiar with the ultrasonic inspection of welds. The usual configuration was 'pulse-echo' in which one probe acted both as transmitter and receiver of the train of pulses. The probe, either held by hand or in a mechanical jig, was scanned over the surface of the component, and the echo signals displayed on an instrument called a 'flaw detector'. The complex way in which the echoes moved as the probe was scanned required skilled interpretation, but when the flaw detector was calibrated in range, the so-called echo-dynamic pattern would distinguish a defect from innocuous echoes and allow its position and size to be measured to an accuracy between, say, ±1 and ±3 mm. This was usually sufficient for finite element stress analysis and materials properties to make a crack growth and fracture assessment of the component, and decide whether the defect should be excavated and the component repaired (not necessarily the best choice) or tolerated and monitored.

I have reported the mathematics behind the triangular tile model in an article on sound radiation on my web site *www.mathstudio.co.uk*. It is entitled 'Physics of sound wave radiation from vibrating surfaces' and is described there in §6 on Kirchhoff theory, §7 where some verification is given, and in Appendix 1 where a derivation of the formula runs parallel to the derivation in Appendix B of the CEGB report below.

The diagrams are from the original report. I have added footnotes to explain NDT technicians' jargon and to remind the reader by the limited computing power available at the time and the constraints it imposed on program coding.

Summary page

CEGB THEORETICAL MODELS OF ULTRASONIC NDT:
'TRIANGULAR FACET' MODEL FOR PREDICTING ECHOES FROM RANDOMLY ROUGH, CRACK-LIKE DEFECTS

by J. M. Coffey, NDT Applications Centre

CEGB Unrestricted report CED/STN/87/20153/R, PWR/IWG/P(87)72

SUMMARY

Theoretical models of practical ultrasonic NDT procedures have been steadily developed at the NDT Applications Centre[2] over several years. The development described in this report contributes to a suite of computer programs for ultrasonic modelling, the others of which deal with smooth flat cracks. This current development provides a fairly simple, approximate means for predicting the ultrasonic signal amplitudes and pulse shapes from postulated randomly rough, crack-like planar defects.

The defect is represented as a mosaic of triangular facets each of which is arbitrarily tilted out of the mean plane of the defect. A pulsed beam from an ultrasonic probe is modelled as illuminating the defect from a specified arbitrary position and direction. The consequent scattering from the defect is calculated in the acoustic Kirchhoff approximation, whereby elementary secondary sound sources on the defect's surface are added together with the appropriate amplitudes and phases. This superposition of secondary waves is done in two stages: i) over each flat facet the signal is found by evaluation of an analytical expression for scattering by a triangle: ii) the contributions of the many triangles are added numerically.

A computer program has been written to calculate the detected signal in pulse-echo inspection, and predicts the full detail of the unrectified pulse. The program and its output are outlined, and several different types of result, including the effects of angle of incidence, range and defect roughness, are presented. These illustrate the range of application of the program towards quantifying defect detection and sizing.

The report discusses the limitations of the theory. Some of these can be overcome by modest development, but others are fundamental and associated with the great complexity both of natural defects and of the way elastic waves reflect at irregular surfaces.

The report also describes how one can obtain representations of crack face structure as mosaics of triangular facets, since such data are essential for input to the scattering program. Crack morphology can be obtained experimentally using the instrument described by Franklin, Schneider and Webster (CEGB Report OED/STN/87/20151/R), or generated in a computer by numerical simulation.

[2] The Non-Destructive Testing Applications Centre (NDTAC) where the author worked from the 1970s to the mid 80s. It was a section within the Central Electricity Generating Board charged with improving the techniques and technology of NDT, though most of its developments used ultrasonics. It was founded and led by its charismatic manager Dr. Graham Oates who promoted combining ultrasonic NDT with fracture mechanics.

CONCLUSIONS

1. An approximate mathematical model to predict the detected from rough cracks has been developed. A been written to deal with the pulse-echo mode of essential features of the ultrasonic inspection, and the defect's size, position, orientation and in the program.

2. Despite some fundamental limitations in the mathematics, the model gives predictions which appear plausible and realistic. Moreover, relevant to defect sizing, there are statistical arguments for believing that the shapes of the predicted echodynamic patterns are broadly correct. Therefore the model is likely to be of significant practical benefit in helping predict the ultrasonic detectability of rough cracks, and the errors in defect size measurement.

RECOMMENDATIONS

1. The model should be verified by comparison with experimental evidence. In the first instance this should involve comparison of the model's predictions with currently available data. Where shortcomings in the experimental data are identified, consideration should be given to a specific programme of experimental verification.

2. In order to allow the model to be applied to actual natural rough cracks, it should be interfaced with the crack surface profile measurements of Franklin, Schneider and Webster (CEGB Report OED/STN/87/20151/R).

Contents

1 Background to the development

Over the last six years Dr. R. K. Chapman of the NDT Applications Centre and the author have been developing theoretical models to predict the ultrasonic signals that would be detected if an ultrasonic probe scanned over a specified defect in an ultrasonic non-destructive test. Models are potentially most useful in inspection design, and in 'validating' inspection procedures, where they complement empirical trials on defective specimens (ref. 1). So far almost all our work has concentrated on smooth flat cracks, and now there is a suite of computer programs established and documented for dealing with most probe/defect configurations by which planar defects can be detected – pulse-echo, tandem, corner effect, edge wave diffraction, etc. A recent paper by Chapman (ref. 2) gives the current position and includes a fairly complete reference list. Smooth cracks are worth studying because

a) some important types of real defect are smooth, including fatigue cracks and some lack of fusion and lack of penetration defects in welds,

b) in circumstances away from specular reflection they may represent a 'worst case', such that if a smooth defect can be detected, then probably most other kinds of defect of the same size would be detected at least as readily,

c) the mathematics is tractable and analytical methods are well established so that one can have confidence that the model predictions are accurate and reliable.

Despite the value of this suite of models for smooth flat cracks, it has long been recognised that a model of rough cracks is also required in order to deal with fundamental questions in the detection and sizing of many natural cracks. Roughness on the crack face is an essential characteristic of brittle fractures, ductile and lamellar tears, solidification cracks, reheat, hydrogen and stress-corrosion cracks, and this list is not exhaustive. Roughness has a profound effect of the ultrasonic response of a crack; it introduces a random, diffuse component to the scattered field which competes for the scattered energy with the specularly reflected component. The diffuse scatter has a much lower amplitude than the specular signal from a smooth crack, but it spreads into a very wide solid angle. This allows rough defects to be detected in pulse-echo testing even when they are misoriented by several tens of degrees from normal incidence. Moreover, in defect sizing and characterisation it is the random diffuse scatter which gives rise to the 'travelling echo' echodynamic, referred to as Pattern 3 in BS 3923 Part 1 and in the ESI Standard 98-10 on ultrasonic weld inspection.

There is a vast literature on scattering from rough surfaces, and much of it describes elegant analytical mathematics – see, for example, the review by Ogilvy (ref. 3). Much of the published material, however, is only of limited application to ultrasonic NDT. Many studies were carried out for naval purposes on scattering from the sea surface and from the sea bed. These, therefore, deal only with surfaces which are effectively infinite in extent, whereas we in NDT are particularly interested in the response from near the defect's edge because of the importance of the defect's extremities in sizing. Again, much of the literature has only plane waves incident, or else a very wide beam from a small hydrophone, whereas our models must deal with quite fine beams and short pulses from NDT probes. Hardly any theory is done on elastic waves; it is practically all acoustic scalar waves though, as is argued in Section 4, this shortcoming is probably not so serious as to undermine the practical value of acoustic models. About ten years ago the author attempted to adapt the analytical method of M.V. Berry of Bristol University[3] (ref. 4) to NDT by building finite defects and a model of the probe beam into Berry's Kirchhoff theory. Little of this was published – only a few graphs illustrating the effect of roughness on signal amplitude (ref. 5). Though the potential benefits of a model of rough defects are great, there are formidable difficulties in producing an accurate model in which all the parameters relevant to NDT are included, as outlined below.

[3]He later was awarded as Sir Michael Berry, FRS

The problems are essentially three-fold: a) crack surfaces are very complicated, b) the pulse-crack interaction is very complicated, and c) the echoes received at the probe are very complicated.

Taking these in turn, anyone who has examined the faces of a broken open rough crack knows that there is structure on several length scales, from the scale of several millimetres down to the microscopic level. Moreover, cracks produced by different cracking processes generally look quite different to the eye. We ask whether this appearance can possibly be quantified simply by a few statistical indices such as r.m.s. height, etc? What are the key features of this surface structure which determine the ultrasonic scattering? These features need to be identified and represented as parameters in any model of scattering from the surface. The paper by colleagues at the NDTA Centre, reference 6, describes studies to quantify roughness more fully.

Considering the pulse-crack interaction, the different length scales on the surface will scatter the incident pulse in different ways, with the large scale undulations producing quite observable range differences and the very fine scale 'tooth' to the surface probably causing only attenuation. The intermediate features, on a scale comparable with the wavelength, will produce a most complicated wave field by diffraction at facets, steps and edges, with mode conversion to bulk and surface waves, with multiple scattering between facets and with shadowing of some-parts on the surface by others. Mathematical techniques are not yet available to deal with this rigorously.

The third area of difficulty is the echoes themselves. Whereas echoes from a smooth flat are few in number and simple in pulse shape (due to either specular reflection or edge diffraction), those from a rough surface form a complex, random pulse train, with many 'subsidiary maxima' in the echo envelope. The echo, like the defect, must therefore be described statistically; one talks for instance, of amplitude distribution functions, correlation functions, or the probability of a subsidiary maximum occurring within x mm of the crack edge. All this makes it more difficult to pull out the technical significance for practical NDT from the numerical or analytical results of any theory. It also means that one specimen cannot give a representative answer; we have to study a sufficient number of statistically equivalent specimens.

Despite these daunting difficulties, some sort of model for the ultrasonic detection and sizing of rough cracks is necessary. It is needed to give physical insight in interpreting NDT results, and to complement the programmes of experimental work under way at the NDT Applications Centre (ref. 7), under PISC III[4], and elsewhere which aim to provide the technical justifications for current and future ultrasonic procedures. This report describes one model which, despite its many approximations and limitations, aims to predict the ultrasonic pulses reflected from a given randomly rough, finite, crack-like defect when examined by realistic ultrasonic probes from arbitrary angle of incidence and from any range; in other words, the model is tailored towards practical ultrasonic NDT. The model was originally developed as

[4] The Plate Inspection Steering Committee coordinated a European program to validate weld inspection for critical nuclear power plant.

a BASIC computer program on a BBC Model B microcomputer, though it has since been translated into FORTRAN by Dr. R.K. Chapman to run on a MicroVAX computer.

A parallel development of acoustic modelling of rough surfaces and rough surface scatter has been made by Jill Ogilvy of UKAEA Harwell (ref. 8). Her model also uses the Kirchhoff approximation and treats ribbed surfaces rough in only one dimension. The wave integral is performed purely numerically. The reader may also note that some time ago N.F. Haines and D.B. Langsten of Berkeley Nuclear Labs. suggested a similar facet model for crack scattering in reference 9, though this seems not to have been developed. This current model has been derived independently.

The structure of this report is as follows. The principle of the model is outlined in Section 2. Section 3 gives some discussion of the computer program as implemented in BASIC on the BBC, since this example shows the parameters which are included and illustrates the progress of the calculation. The reader having become thus acquainted with how the model works, we move on in Section 4 to outline its limitations, its likely realm of validity and the steps which might be taken in future to remove limitations or to improve its accuracy. In Section 5 we leave the model of scattering itself and discuss the production of data on crack face roughness which forms the essential input to the scattering program. Some of these data can come from experimental measurements on crack specimens; others can be generated by computer simulations of rough surfaces using random numbers. The final main section, Section 6, contains some short illustrative examples of the type of application that the model has in the areas of crack detection and sizing. Appendixes contain further detail of the scattering calculation, the generation of artificial rough surfaces, the treatment of shadowing and the calculation of some elementary statistics on these rough surfaces.

2 The 'triangular facet' model: principles

The principle of the model is simply stated. The defect's surface is regarded as being made up of irregular triangular facets. The triangles fit together along adjacent sides, like a mosaic of triangular tiles, but are each tilted out of the mean plane of the surface in a random way. The projected shape of the overall defect can be selected to be circular, elliptical or rectangular. Figure 1 is an artist's impression of the defect and probe and shows the type of defect intended. A pulse (or alternatively a beam of continuous waves at the pulse's centre frequency) from the pulse-echo probe strikes the defect. The signal in backscatter at the probe is calculated using Kirchhoff theory. So far this is acoustic Kirchhoff theory, but in principle it could be done elastically as outlined in Section 4. In Kirchhoff theory the scattered signal back at the probe is represented as the sum or integral of wavelets contributed by many infinitesimal 'secondary sources' distributed over the surface of the defect, following Huygens' Principle. In our model the Kirchhoff integration is done in two steps. The first step takes each triangular facet in turn and calculates the contribution it makes back at the probe. This is done by evaluation of an analytical expression which assumes that the incident field is constant over that particular facet. The second step is to add numerically the contributions from each facet, weighting each contribution to allow for the facet-to-facet variations in amplitude across the incident beam

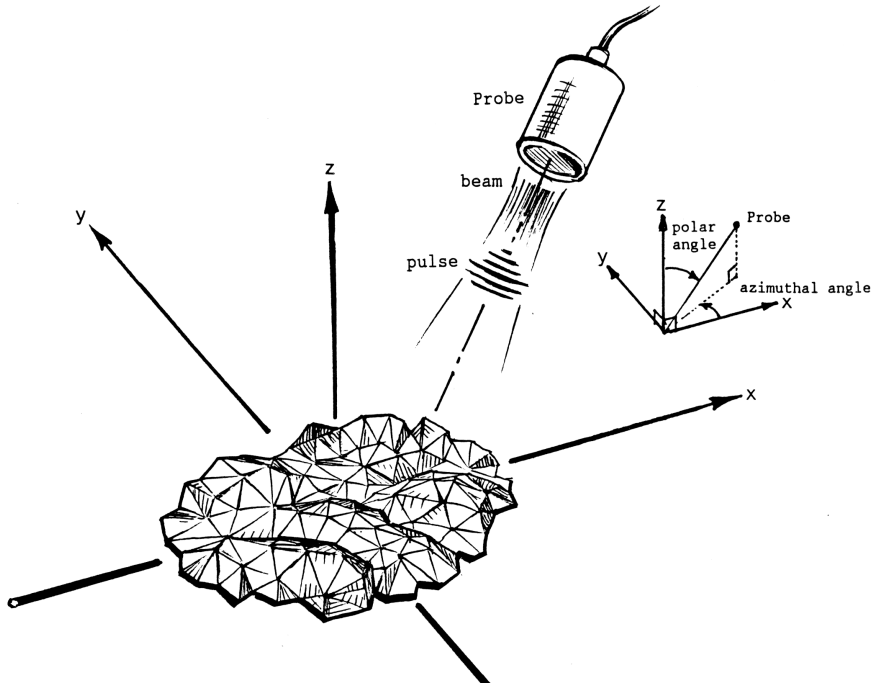

Figure 1: Persepective sketch showing pulsed beam from pulse-echo probe incident on horizontal planar rough crack with a surface structure of triangular facets.

and taking due account of the phases and time of flight of the pulse. The result of this sum is the pulse from the defect as a whole, and its amplitude and shape can be readily displayed.

The facet model can be looked at in a rather different way. In principle the Kirchhoff integral of secondary sources can be evaluated for any non-re-entrant shape of surface. For instance, Ogilvy (reference 8) carries out the integration entirely numerically. In general, one often finds that the phase variation across any facet is large, particularly at oblique incidence. To achieve tolerable numerical accuracy, the interval of digitization in the integral has to be smallâ€"say about 1/10 wavelength. However, much cancellation takes place amongst the values at the many mesh points. Now the Kirchhoff approximation is not reliable when the structure of the surface is on a scale small compared to the wavelength, so there is no justification for trying to represent any structure to the roughness on the scale of 1/10 wavelength. The device of splitting the surface into contiguous triangles, each just over a wavelength in size, allows the fine scale integration to be done analytically and hence exactly (within the terms of the Kirchhoff approximation), and at the same time discourages us from applying Kirchhoff theory to rough surface structure on an unjustifiably small scale.

The first stage in calculating the back scattered field is to evaluate the contribution from each triangle in turn. The triangle is specified by the three spatial co-ordinates of each of its three corners. These are referred in the first instance to a co-ordinate system (x, y, z) fixed with respect to the centre of the defect as a whole. The position of the probe will also have been specified by the user in this global co-ordinate system. To calculate the wave-facet interaction we use co-ordinate local to that particular triangle. Viewed from this local co-ordinate system, the triangle appears to be horizontal, co-ordinates at the centroid and the

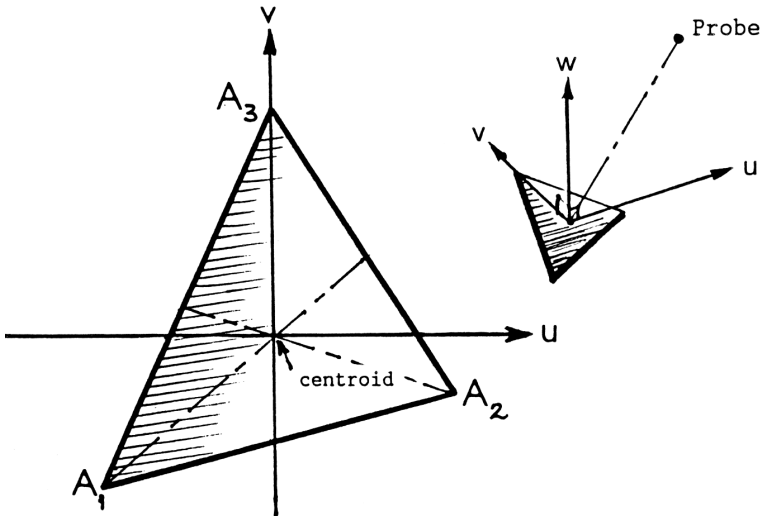

Figure 2: A single triangular facet lying in the (u, v) planbe of the local (u, v, w) co-ordinate system with centrold as origin.

probe at some distant (Figure 2). The probe's co-ordinates in this local system are evaluated. The global and local co-ordinate systems are related by a transformation as described in Appendix A.

Since the facet is small compared with its distance from the probe, the incident beam will look like a uniform plane wave over the facet. The Kirchhoff integral representation of the diffracted signal from a general reflector is well established and found in standard books on light and sound (see for example, references 10). It is quite straightforward to evaluate this wave integral analytically over the triangle for an incident continuous (single frequency) plane wave of unit amplitude, provided the local 'facet' co-ordinate system is used. Details of this algebra are given in Appendix B. The resulting expression includes the 'obliquity factor' which is the projected area of the facet as seen on looking down the probe beam. The expression evaluates to a complex number $A\exp(i\phi)$ which describes the amplitude and phase of the facet's contribution to a unit incident wave. Clearly this must be weighted to take into account the actual amplitude and phase of the incident wave, as described below.

There are two ways in which the program adds the contributions from all the facets, weighting each according to range and to the field of the probe. The range from the centre of the probe to the centroid of the facet is readily calculated exactly by Pythagoras' theorem. The path length in pulse-echo inspection is twice this. In one calculation the probe is treated as operating with continuous waves. With this the path difference to the defect and back needs to be determined only modulo 2π since it affects only the phase of the signal from the facet. In the other treatment, the probe sends out a short pulse of sound; here the time of flight is retained explicitly and used to displace the contributions from each facet relative to the others in time (*ie.* in range). The two methods give essentially identical values of peak pulse amplitude at normal incidence. For the continuous wave treatment, interference of the waves from all the facets is determined entirely by their phases and amplitudes. However, in the pulsed case interference also depends on the degree to which the pulses from the different

parts of the surface overlap, since the nearer facets contribute to the leading part of the scattered pulse train, and the further parts to the tail. For this reason, at oblique incidence, the calculated overall amplitude for continuous waves is generally not equal to the peak signal in the pulse calculation.

As we have remarked, the contribution from each triangular facet is weighted according to the beam of the ultrasonic probe. The model of beam shape used is that devised by the author some years ago and described in references 11 and 12. A short resumé of this beam model is given in Appendix C. Recent experimental work by Wein and Burch of UKAEA Harwell (to be published) shows that this model is quite realistic and accurate, certainly for ranges at and beyond the nearfield length.

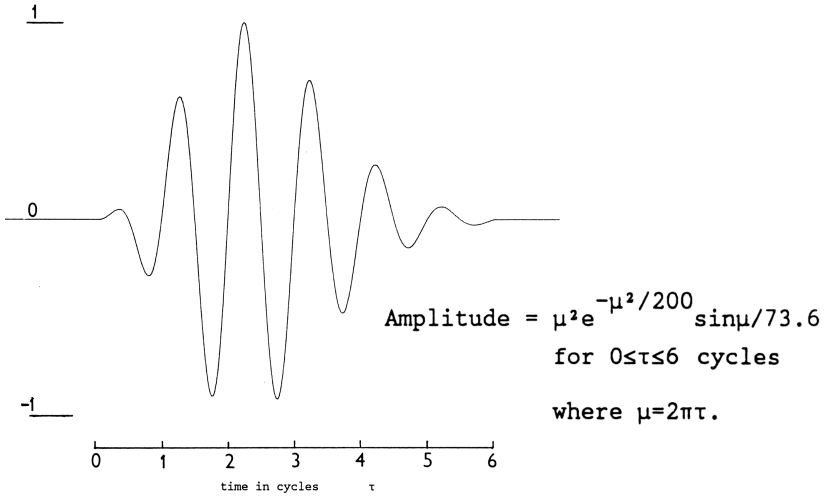

Figure 3: Shape and mathematical expression for the model pulse from probe.

For the pulse treatment outlined above, a reasonable-looking pulse shape is assumed. This is illustrated in Figure 3. At present it is assumed that the incident pulse shape is the same at all positions within the beam. The fact that scattering from each individual facet is calculated assuming continuous waves means that the pulse shape is not changed at all on being scattered by the facet. Neither assumption is quite accurate for reasons discussed in Section 4, but this is a good first approximation.

The only other quantities in our model whose influences on the signal amplitude are currently included are the reflection coefficient at the defect and the shadowing of one part of the surface by another. For back scatter (and only back scatter) the elastic reflection coefficient is identically unity – this remarkable fact is proved by Dr. Chapman in reference 12. Hence no special effort is needed to cope with the reflection coefficient. Shadowing is more complicated. A thorough (but still not rigorous) treatment would involve tracing the ray from the probe to each facet and determining whether it intersected any other part of the surface. This is rather like the problem in the computer graphics of three-dimensional objects where hidden lines have to be removed. In the program so far this facet-by-facet approach to shadowing has not been followed. Rather the signal amplitude from the defect as a whole is calculated first by largely neglecting shadowing, and then multiplied by a single factor derived

by Wagner (ref. 13) which corrects approximately for the average effect of shadowing. The treatment of shadowing is discussed in more detail in Appendix D.

Putting all these steps together, the signal from the defect can be expressed mathematically as follows:

Continuous Wave Calculation: For N illuminated triangles, (*i.e.* ones for which the obliquity factor is greater than 0), each denoted by j and having centre c,

$$\text{C.W. Signal} \;\propto\; \frac{S_w}{1-F_s}\sum_{j=1}^{N}(\psi^{inc}(c_j))^2\,A(c_j)[\mathbf{e_s}(c_j)\cdot\mathbf{n_j}]$$

$$\text{where}\quad A(c_j) \;=\; \iint_{\Delta_j}\exp[ik(uS_u+vS_v)]\,d\Delta_j. \tag{1}$$

following the notation of Appendix B. $\psi^{inc}(c_j)$ is the field incident on the centroid of the jth triangle. S_w is Wagner's shadowing function and F_s the fraction of facets for which the obliquity factor is not greater than zero (Appendix D).

Pulse Calculation: Signal at time t is proportional to

$$\frac{S_w}{1-F_s}\sum_{j=1}^{N}|(\psi^{inc}(c_j))^2\,A(c_j)[\mathbf{e_s}(c_j)\cdot\mathbf{n_j}]|\,P(f_0t-\delta_j)$$

$$\text{where}\quad \delta_j \;=\; \frac{2R_j}{\lambda_0} \;+\; \arg\left(\frac{A(c_j)}{2\pi}\right), \tag{2}$$

f_0 being the centre frequency of the pulse, λ_0 the corresponding wavelength and $P(t)$ the incident pulse shape shown in Figure 3.

3 Illustration of the computer program

3.1 Setting up the calculation

As mentioned before, the model was originally coded as a program in BBC BASIC to run interactively on a BBC micro computer. This section briefly describes the features of the program from a user's point of view. By this example the reader may gain a clearer picture of what the model does, and of the parameters whose values may be selected to represent different situations of interest in NDT. The results output by the program are the continuous wave amplitude and also the pulse shape (obtained by the two parallel calculations described in Section 2) corresponding to the probe at one selected position with respect to the defect. To simulate scans, the calculation by equations I and 2 must be rerun for each position in the scan. The VAX FORTRAN version of the program prepared by Dr. Chapman gives similar output, but without the graphics. Both versions give the same numerical values.

Figure 4 illustrates the type of defect which is dealt with. Figure 5 is an example of the first page of the input/output during which the calculation is set up. Figure 6 shows the BBC screen display during the course of the calculation.

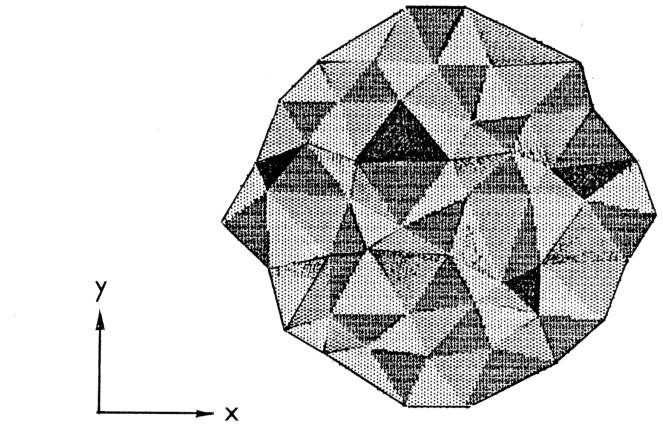

a) Plan view of approximately circular defect

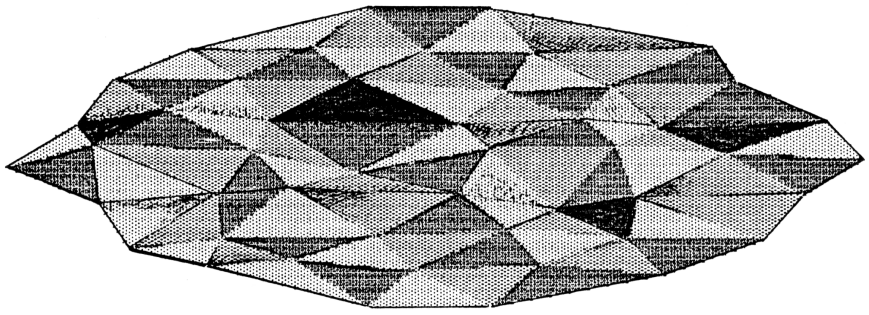

b) elliptical reflector with anisotropic facets produced by scaling circular reflector in (a) by ×2 in x, ×¾ in y.

Figure 4: Plan views of simulated defects showing effect of x and y scale factors.

On starting a RUN (Figure 5) the user is asked to enter the name of a data file which holds the co-ordinates of the corners of all the triangles which make up a defect. This file would have to have been created previously using one of the methods described in Section 5. The defect data file has a header, giving crack size, facet size and statistics, *etc.*

The next step is to decide whether you want to scale the defect in any of its three dimensions. You can select to multiply the x, y and/or z co-ordinates by separate arbitrary constants. The co-ordinate system is shown in Figure 1. The effect of scaling x and/or y is simply to enlarge or shrink the projected size and shape of the defect. This can be useful in seeing the effect of changes in size and shape. If the x scaling is different from the y, not only is the defect shape changed (a circle becoming an ellipse, say), but the facets become stretched; this simulates a surface anisotropy. Figure 4a is a plan view of a circular defect, and 4b shows the anisotropic elliptical defect produced by scaling in x by 2 and in y by 3/4. Isotropically rough elliptical defects can be generated by the methods of Section 5. The z scaling clearly determines the roughness. In particular, if zero is entered, the surface becomes smooth. One type of application described in Section 6 is to look at the effect of increasing surface roughness on defect response. This is done simply by looping over the z scaling factor, increasing it each time round.

```
>RUN
       Simulation of Scattering from a Rough Surface of Triangular Tiles
                 PART II -- Calculation of the scattering
*******************************************************************************

The surface of triangular tiles must first have been generated using Z.TRTILE1
 and stored in a file.
Enter name of file of surface triangles: Q.CIRC004
With this version you can have up to 100 triangles in the defect.

Please be patient while the data file is read into memory.

Circular reflector, radius 3.000 mm.
Triangular elements: basic side 1.000:    y stretch factor = 1.000
Randomness : Standard Devns. in x,y,z are 0.150,  0.150,  0.150
Do you want to scale the surface dimensions (Y/N)? : Y
Enter x scale factor : 2
Enter y scale factor : 1.5
Enter z scale factor : 1.3

Choose materials : a) water to steel, b) water to plastic,
c) steel to vacuum (P waves), d) steel to vacuum (S waves) : D

Enter properties of probe:--
   Frequency (MHz) and crystal radius (mm) : 4,5
   Wavelength is 0.807 mm.    Nearfield 30.960 mm.    Wavenumber 7.781 /mm.
Enter polar and azimuthal angles of beam axis in degrees : 20,0
Do you wish to enter probe's range or z co-ordinate (R/z) ?: R
Enter range : 50
Choose to enter beam axis position wrt defect centre in
polar (P) or Cartesian (C) co-ordinates : C
Enter beam axis x & y displacements from centre of defect (mm) :  -2,0
Co-ordinates of probe are : x=15.101   y=0.000   z=46.985
Response from eqivalent smooth circular reflector at normal incidence;
Complex signal is 36.872 + i* -35.750
Modulus of signal is 51.358 or 34.212 dB.
```

Figure 5: First page of input/output of BBC BASIC program Input is shown in a box.

Having specified the defect, we have to specify the probe frequency and crystal radius, and its position and orientation with respect to the defect. The sound velocity is selected by choosing the wave mode and the medium in which the sound is travelling – for example, compression waves in water, or shear waves in steel. Given this information, the program computes and displays the wavelength and nearfield length of the probe beam.

The program asks whether you want to specify the range from probe to detect or the z co-ordinate of the probe – that is, the height of the probe above the plane of the defect. If one is simulating a scan across the defect, the z co-ordinate option might be more convenient. One is also asked for the orientation of the probe with respect to the plane of the defect. This is specified to two angles in spherical polars: the polar angle, which is equal to the angle of incidence, and the azimuthal angle with respect to the positive x axis (Figure 1). The last parameters to be input are the displacement of the beam axis, in millimetres, from the centre of the defect, and the azimuth in which this displacement is made. Alternatively, you can enter the Cartesian (x, y) co-ordinates at which the geometrical beam axis intersects the defect. These options allow the probe to be placed at an arbitrary position. The VAX version allows one to specify the probe position and orientation with respect to a steel component which has a flat scanning surface. In this case the beam angle and skew of the probe are entered as parameters.

3.2 Illustrative displays and output

Before the program begins calculating and summing the signals from each triangle, an auxiliary calculation is carried out. This is to evaluate an analytical expression given in Appendix C.2 for the equivalent flat-bottomed hole response of the defect at normal incidence (DGS/AVG response). The result of this preparatory calculation allows the user to relate the signal amplitude of the rough defect to a flat-bottomed hole[5].

To inform the user of the progress of the main calculation, the BBC computer produces two plots (Figure 6), one on either side of the screen. On the left hand side we have a view onto the defect surface – that is, onto the (x, y) plane. As the calculation moves on to deal with another facet, the triangular projection of that facet is plotted in a distinctive colour. Thus the shape of the defect is gradually built up on the screen as a patchwork of triangles. Figure 6 is an example of this screen display when the calculation is about 80% complete.

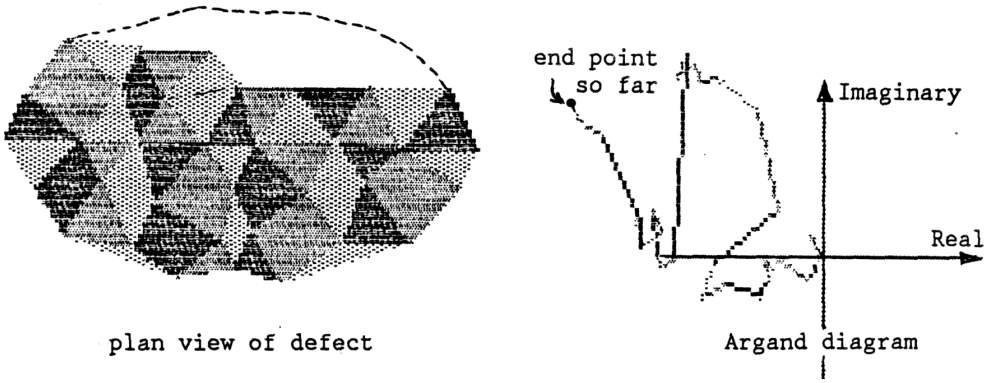

Figure 6: Screen dump at stage when calculation is 80% complete.

Simultaneously to the right of the screen (Figure 6) an Argand diagram is plotted to show the amplitude and phase of the wave contributed by each facet. In this the in-phase and quadrature axes of the phase are drawn, and for each facet a straight line is added whose length is proportional to amplitude and whose direction represents the phase. The amplitude and phase values for this plot are taken from the continuous wave part of the calculation described in Section 2. The line for the current facet adds onto the end of the line from the previous. The line (not plotted) from the centre of the plot to the end of the last added line represents the amplitude and phase of the total defect signal. One observes that for smooth defects the Argand diagram shows a line which is almost straight. This is characteristic of coherent scatter because the contributions from the different facets are all in phase and the drawn lines have the same direction. For a rough defect the phases are quite different and the resulting line is a random walk. For all its length, its end point is not very far away from the origin. The extent to which you can call the line 'straight' is a measure of the coherence of the signal and hence of the roughness of the defect in ultrasonic terms. The contrast between

[5] A series of flat-bottomed holes are various ranges was a set of reference reflectors widely used to calibrate signal amplitude. Each was literally a hole of, say, 4 mm diameter drilled into a block of low-attenuation steel and made flat-bottomed by grinding the drill bit flat. The pulse-echo probe would strike them at normal incidence. They approximated ideal disc reflectors.

rough and smooth defect signals is shown in the Argand diagrams in Figure 7. In this figure the scales are arbitrary – the relative size of the graphs does not imply relative amplitudes.

When the last triangle has been added, four items of information are written to the screen: a) the signal from the defect according to the continuous wave calculation, b) the largest peak in the pulse, according to the time-dependent calculation, c) the range to the peak in the pulse, and d) an estimate of the root mean square height of the surface in millimetres. For example, the output from the case in Figures 5 and 6 is

Amplitude of c.w. signal is $8 \cdot 07$ dB.
Peak rf signal is $1 \cdot 74$ dB.
Range to peak is $50 \cdot 50$ m.
RMS defect height : $0 \cdot 39$ m

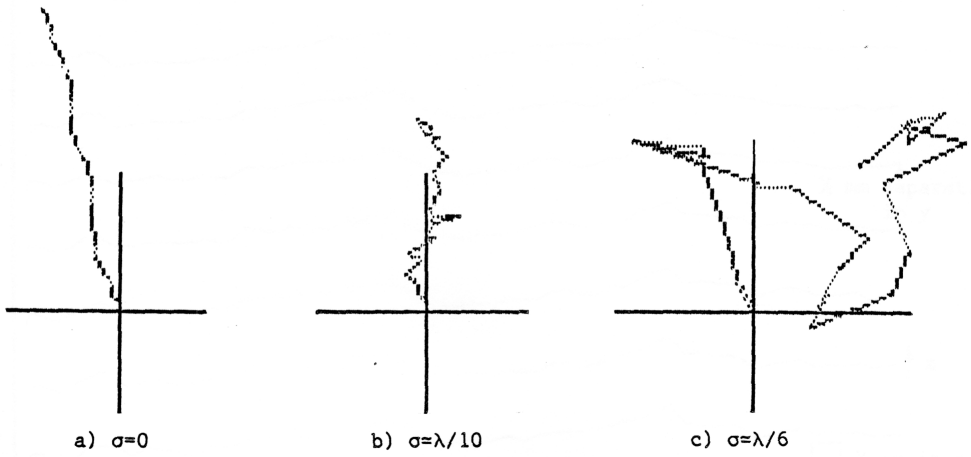

Figure 7: Argand diagram of back-scattered signals for a) smooth, b) intermediate and c) ultrasonically rough reflectrs. Illustration for defect 6 mm diam. 0° incidence with a 4 MHz compression wave probe. σ = rms height (Figures not on the same scale.)

The calculation of roughness is done by adding the variances of all the individual facets, measured from the (x, y) reference plane, and its enlarged upon in Appendix E. Items a) and b) will be similar if the received pulse train is not so spread in range that the head cannot cause destructive wave interference with the tail. In the example above they are over 6 dB different which indicates that the received pulse is substantially elongated. The unrectified signal can also be displayed, as shown in Figure 8.

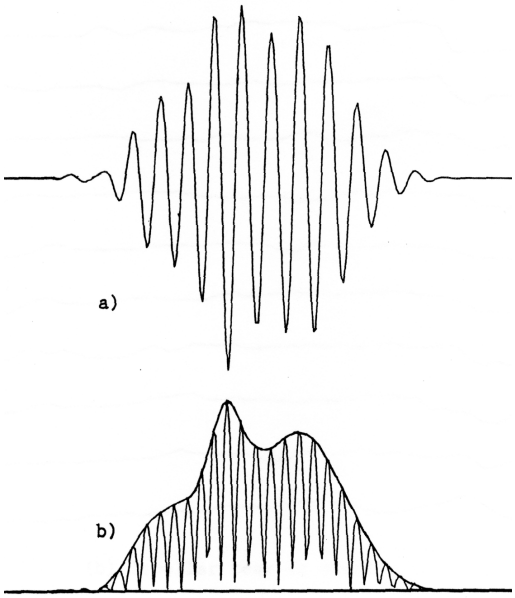

Figure 8: Predicted pulse shape for case in Figure 5. a) rf. signal. b) rectified signal.

4 Range of validity and scope for development

From the description given and from the examples in Sections 3 and 6, the reader may be satisfied that the program 'gets an answer'. The predicted pulse shapes and signal amplitudes may be plausible, but unfortunately this does not mean that they are necessarily a faithful description of reality. The shortcomings and limitations described in this section fall into two classes:

a) those which are limitations of the program as developed to date, but which it would be straightforward to improve upon with a modest amount of effort, and

b) those that are quite fundamental and where there seems little hope for making improvement in the near future.

These two classes are discussed separately below. Appendix F deals with the 'quality assurance' of the program as it stands. As a general point, it is clearly necessary to verify the theory and define its range of validity by comparison with experiment.

4.1 Some current but surmountable limitations

One tractable development would be to replace the continuous wave calculation of scattering from an individual facet by a time-dependent calculation. One approach here is to regard the incoming field as being a very short pulse, like a δ-function. The response of the facet to this would also be a short pulse, but with some internal structure due to scatter from the face and three edges of the triangle. Convolution of this δ-function response with the incidence pulse train of Figure 3 would give a more realistic approximation to scattering of the pulse from a facet. To take advantage of this a similar extension of the probe beam model to the time-dependent case would be necessary. An alternative and possibly more

easy approach would be to combine contributions over a range of frequencies as a Fourier spectrum, evaluated numerically. This is the approach followed in some recent developments of the NDTAC computer programs for smooth cracks to an explicit time dependence (see reference 14).

A further development would be to convert the calculation from acoustic scalar waves to elastic waves, but still within the Kirchhoff approximation. This is more easily done for the time-harmonic case than in its full time dependence. Elastic waves are vector waves, so the rays incident on each facet must be characterised by a polarization vector as well as a ray direction. The plane of polarization, which is established by the beam axis and surface normal under the probe, will be rotated by reflection from each facet. The amount of rotation will differ from one facet to the next depending on the orientation of each facet. The ability of the probe on reception to respond to the incoming wave contributions will depend on their polarization with respect to the probe's own polarization axis, the response falling as the cosine of the angle of deviation.

As noted previously, the elastic reflection coefficient in back scatter is 1, so for pulse-echo inspections no further modification needs making other than to change to vector waves. A rather more long term development might include additional probe configurations, such as tandem and the corner effect. However this would require the elastic calculation of the Kirchhoff expressions for the two-probe scattering from a triangle for compression (P) waves and the two polarizations of shear waves (SV and SH). This involves the elastic Green's tensor and the plane wave reflection coefficients, and follows the methods described by Chapman in his report on Kirchhoff theory for smooth flat cracks, reference 12. The main difficulty would be the tensor mathematics. The limitations of Kirchhoff theory discussed in 4.2 would, of course, remain even in the elastic case, but at least the model would be more overtly realistic.

4.2 Fundamental difficulties

There are two big fundamental limitations of the model. One is the model of the surface – do real surfaces really look like triangular facets? The other is the limited confidence which can justifiably be placed in Kirchhoff theory for dealing with such complex scatterers, especially when they have structure on the scale of the wavelength. When examined with a magnifying glass, facets can be seen on the face of a brittle fracture. A few other defects have a facetted surface structure, but in almost all cases there is structure on the crack on length scales from several millimetres down to microns, well below the ultrasonic wavelength. The 'triangular facet' model has an in-built cut-off to how much fine scale structure it contains, set by the average size of the triangles. In this respect it is unrealistic. Kirchhoff theory, however, is a high frequency approximation and so its accuracy is favoured by having large facets – say, two or more wavelengths across. But, this is contrary to the requirement from modelling surfaces realistically. In the calculations carried out so far with the model, we have chosen the triangles to be about one wavelength across, hoping this is a reasonable compromise. Note, however, that this is a limitation of all formulation using the Kirchhoff approximation, and not some peculiar weakness of the current model.

A speculative development might be to try and represent the individual triangles as having a fine scale roughness upon them. The effect of this on scattering might be estimated using some appropriate theory (not Kirchhoff) or even using empirical values obtained from measurements on grit blasted flat specimens, say. The inherent limitations of Kirchhoff theory are well recognised and discussed by Chapman (reference 12). It becomes increasingly inaccurate as the facet to wavelength size decreases, it neglects production of Rayleigh surface waves on the defect (even in the elastic formulation) and it neglects multiple scattering from one facet to the next. In our model all the facets are treated as independent and non-interacting. This assumption of non-interaction is particularly dubious in elastic scattering because Rayleigh waves will clearly creep over the surface, linking one facet to many others. We use Kirchhoff theory not because it necessarily is a good approximation, but because it is currently about the only tractable approach.

Lest this seems too negative, we can take comfort from the Central Limit Theorem of statistics which says that the sum of the waves from the many scatterers tends to be Gaussian in distribution, irrespective of the detailed nature of the scattering. This means that the model will probably give about the right answer for some of the important statistics of the echoes even though the values of the amplitudes may be unreliable and some results for any individual rough defect may be wildly out. Fortunately much of the interest in ultrasonic NDT is in the statistics rather than the individual cases. For example, we are interested in the *typical* behaviour of echodynamic patterns and the *average* accuracy of defect sizing. The amplitude fluctuations in each pattern as the probe scans are likely to be represented quite well by this model because the spatial variation results from the interference of many facets so the statistics should not depend critically on the precise details of the surface. Therefore the model is likely to be good in determining errors inherent in the defect sizing techniques such as Maximum Amplitude, 20 dB Drop, *etc* [6]. It may be less reliable in predicting the detectability of defects with respect to a threshold. Even so, we might expect it to give the correct trends and so be valuable in interpolating between experimentally determined values. As stressed above, it clearly needs verification by comparison with carefully designed experiments, especially in regard to the predicted signal amplitudes.

5 Some models of rough surface structure

Up till now we have said little about the structure assumed for the defect's surface beyond making it clear that the model for scattering requires it to be a mosaic of triangular facets. The scattering computer program reads in the nine co-ordinates of each triangle's corners, triangle after triangle, from a data file created previously. In this section and its related appendices we discuss some means by which these data files of co-ordinates may be obtained.

[6] These names had been given in the 1960s to practical recipes for measuring the size of a crack. Each involved placing the ultrasonic probe so that the last maximum was found as the probe travelled off the defect at either end. The maximum amplitude method assumed that the beam centre was then passing through the edge of the defect. The 20-dB drop method would scan until the signal dropped to 1/10 (20 decibels down) on this maximum and then assumed that the 20 dB beam contour (as calibrated on drilled holes in a calibration block) was passing through the defect's edge.

There are three aspects to this:

a) choosing the (x, y) co-ordinates of the vertices – that is, the projections of the vertices in the plane of the defect,

b) obtaining the heights, z, above and below this plane, and

c) deciding how the separate vertex points are to be connected so as to form triangles.

Though aspects a) and c) are largely a matter for our choice as discussed below, the heights, b), can be obtained either experimentally or by numerical simulation. We first outline one experimental method.

5.1 Experimental determination

In order to measure the profiles of broken-open crack faces, a special instrument has been designed, built and commissioned at NDTAC[7]. It is described fully by Franklin, Schneider and Webster (ref. 15), and the analysis of surface profiles measured using this instrument is being currently dealt with by Schneider (see ref.6). Its principle is simple. A needle is lowered under pneumatic action onto the specimen's surface. The displacement in the z direction of the needle's point from a horizontal reference plane is measured to micron accuracy by a Linear Variable Displacement Transducer (LVDT), and the result recorded via a micro-computer onto floppy disc. The LVDT with its needle is mounted on a small motorised carriage under the control of the computer. When one point on the surface has been measured, the carriage is incremented in x or y through typically 50 to 200 microns, and the process repeated. In this way the surface height is measured over a fine rectangular raster relative to the horizontal reference plane.

There is one complication: the reference plane, which is fixed by the construction of the measuring machine, in general is not parallel to the mean plane of the crack surface, which depends on how the specimen is clamped in the instrument. Indeed, on a very rough specimen there is genuinely some ambiguity as to what we should identify as the 'mean plane'. The procedure adopted is to fit a least squares plane to the measured height values, and subtract the value of this from the measured value, for each measured point. Figure 9 is a 'waterfall plot' of adjacent scan lines over two rough cracks, compensated for mean surface slopes.

As noted, currently the instrument is set up to collect height values on a rectangular raster. There is no unique way for joining up such points into sets of three to represent contiguous triangles. As Figure 10a illustrates, arrangements A and B are equally reasonable. C is a more elaborate version of these. Arrangement D is also possible, but not so plausible. Currently a program is being written to convert the measured point values into facet data

[7] The concept for this instrument was the author's, specifically to meet the needs of this topic. I had previously considered alternative methods for measuring crack roughness, including optical methods, but none seemed satisfactory. Construction and commissioning of this direct point-by-point instrument was managed by Mr. Peter Webster.

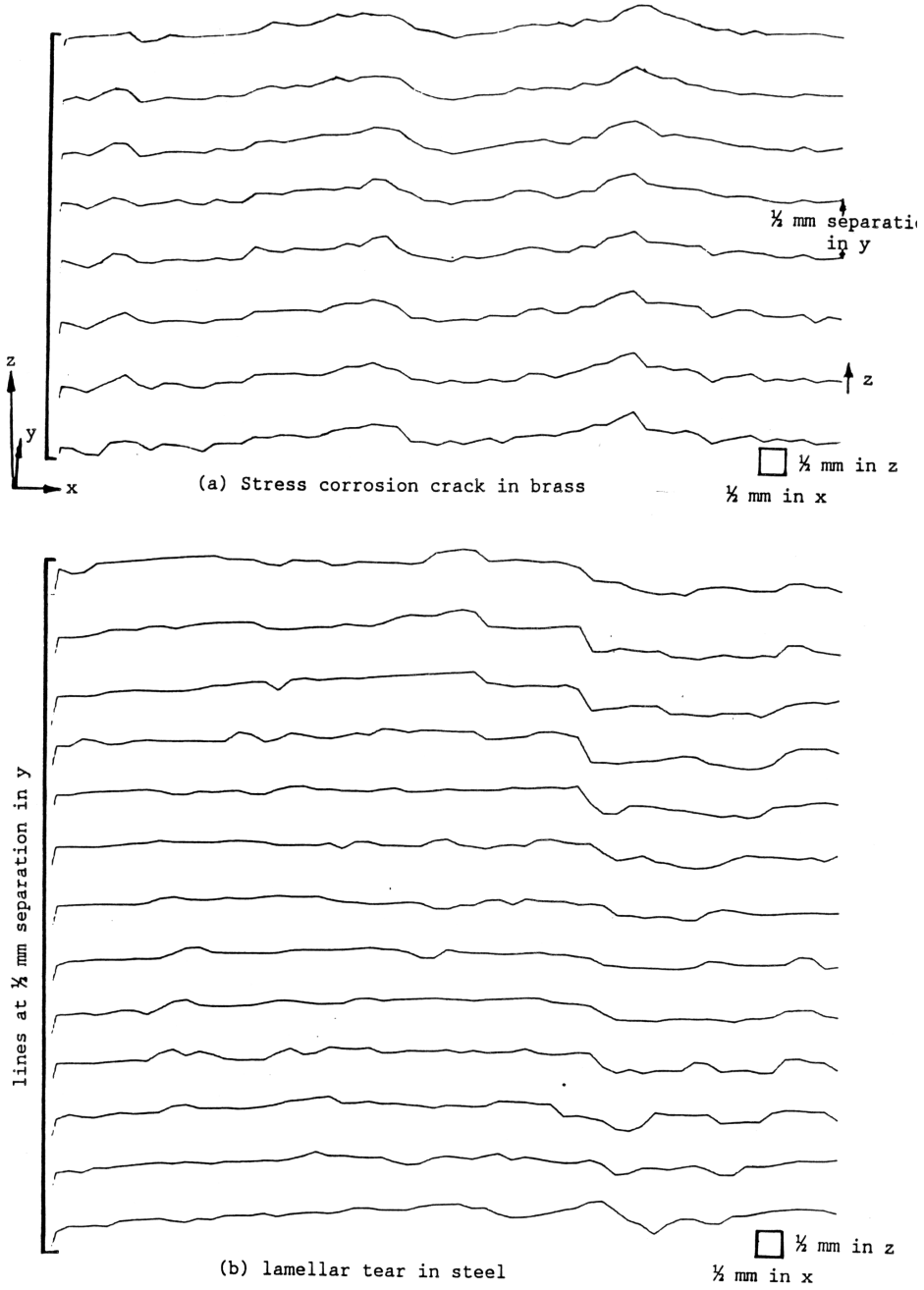

Figure 9: Waterfall plots of surface profiles of two rough cracks measured on a $\frac{1}{2}$ mm raster using the instrument of Franklin, Schneider and Webster. Scale $\times 5$ in x and z: y separation of lines $\frac{1}{2}$ mm.

files according to schemes A and B. The surfaces of triangles fitted by A and B will differ from one another and, indeed from the actual rough surface specimen. The intention is to run the scattering program for both the A and B configurations in Figure A. The extent to which both sets of predicted signal amplitudes and pulse shapes agree will be an indication of the ability we have to interface the scattering model with real defect surfaces.

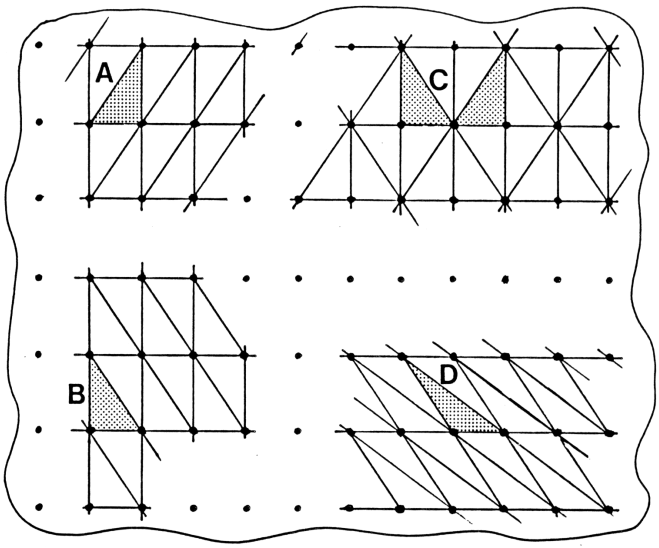

Figure 10: Schemes for the representation of experimentally measured crack surface a mosaics of triangular facets.

5.2 Numerical simulation of triangular facets

All the calculations of rough surface scattering performed so far, including the examples in Section 6, are based on the computer simulations of surface structure described here. The author has written a program in BASIC, running on the BBC microcomputer, to generate data files of triangles specifically for input to the scattering program described in Section 3. A brief description of this program is given below. The advantage of numerical generation of surfaces is that one can produce a very large number of surfaces with the same statistical properties, and hence numerically obtain statistics on the echoes.

In the facet-generating program, the user enters the desired shape and size of the defect – circle, ellipse or rectangle. The 'defect' produced by the program will, of course, be an irregular polygon which approximates to this selected circle, ellipse or rectangle. The program next covers the 'defective' area with a grid of points whose positions correspond to the vertices of identical adjacent isosceles triangles, as shown in Figure 11. The user can choose the size of the base of these triangles and their perpendicular height. Equilateral triangles give the most isotropic surface texture, though the surface can be given a structural anisotropy by having either very pointed or very squat isosceles triangles. Note that some triangles around the perimeter of the defect are not isosceles. These are included to improve the fit of the polygonal perimeter to the notional circle, ellipse or rectangle.

This grid of isosceles triangles is not displayed or recorded; rather the program goes on to derive a sequence of (x, y) co-ordinates representing the projected vertices of irregular contiguous triangles covering the same region. These are derived from the (virtual) isosceles triangles by adding random numbers Δx, Δy to the x and y co-ordinates from Gaussian distributions centred on $\Delta x = 0$, $\Delta y = 0$. The typical structure at this stage is illustrated in Figure 4. It is found that the standard deviation of Δx or Δy can go up to $0 \cdot 15$ or even $0 \cdot 2$

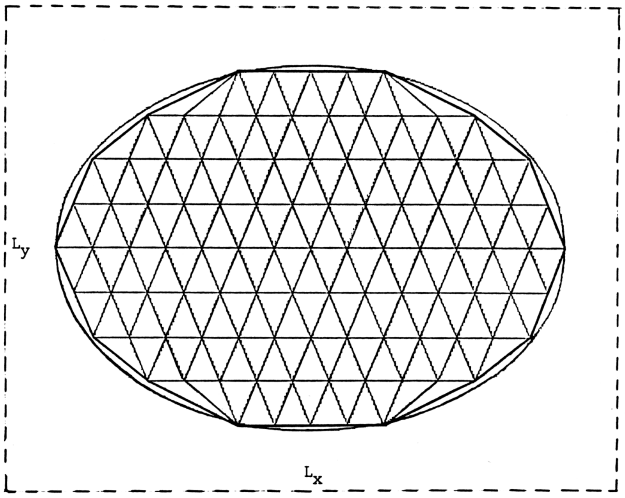

Figure 11: Isosceles triangles arranged over an elliptical defect 7×5 mm. Each triangle is 1 mm base $\times 1 \cdot 4$ mm high. The enclosing rectangle represents the units cell which would be covered in this case by the double Fourier series in Eq. 3.

times the base or height dimension of the underlying isosceles triangles without the derived irregular triangles overlaying one another. Clearly such overlaying would occur if the random numbers added to the vertices were large, and such a state would represent a surface with re-entrant features. However, it is beyond the capability of Kirchhoff scattering theory to cope with re-entrant surfaces.

The program provides five options for generating the height displacements, Δz, of the vertices, though these are derived from only two distinct principles:

i) the allocation of an independent random number at each vertex, and

ii) the allocation of a number obtained from summation of a two dimensional Fourier series with random coefficients.

In (i) the independent random numbers are distributed about zero height and are produced by a Gaussian random number generator, the standard deviation of which is specified by the user. These numbers are quick to generate but, being totally independent, produce a surface where the heights are uncorrelated from place to place. Such surfaces appear to be macroscopically flat, with a distinct fine-scale 'tooth'.

The alternative approach of representing the surface heights as a two dimensional Fourier series imposes a correlation amongst the height values through the lower spatial frequency components. This gives the surface more 'geography'. The Fourier series used is of the form

$$\sum_{i=0}^{N_x/2} \sum_{j=0}^{N_y/2} W_{ij}[\, A_{ij} \cos(\omega_i x) \cos(\omega_j y) \;+\; B_{ij} \cos(\omega_i x) \sin(\omega_j y) + C_{ij} \sin(\omega_i x) \cos(\omega_j y) \;+\; D_{ij} \sin(\omega_i x) \sin(\omega_j y)\,] \qquad (3)$$

where $\omega_i = 2\pi i/L_x$, L_x being a distance somewhat longer than the longest dimension of the defect in the x direction, and L_x/i is the x-wavelength, and similarly for j in the y direction[8]. The coefficients A_{ij}, *etc.* are random, having a mean absolute value of 1, an approximately Gaussian spread about this mean with $\sigma = 0{\cdot}4$, and arbitrary sign (*i.e.* + or −). N_x and N_y are approximately the number of facets along the x and y dimensions of the defect respectively at its widest places. There are therefore $4\left(\frac{N_x}{2}+1\right)\left(\frac{N_y}{2}+1\right) > N_xN_y$ independent random numbers in generating a surface of N_xN_y facets. The division by 2 in the upper limit of the summation occurs because the shortest spatial wavelength can, by the Nyquist sampling theorem, represent two independent numbers which are an interval of half this wavelength apart. Figure 11 illustrates that in counting N_x , one must recognise that **two** triangles are fitted to each base. The dimensions L_x and L_y define a rectangle into which the projection of the defect will fit. In the calculation, L_x and L_y are chosen to allow a margin round the defect. This is in order to make the left and right ends, and the top and bottom edges, substantially independent of one another, bearing in mind that Eq 3 gives a pattern which repeats every L_xL_y.

The weight functions W_{ij} are wavelength dependent and can be selected by the user. The 'waves' of spatial structure in the surface corresponding to x and y-wavelengths L_x, L_y have crests at angle $\tan^{-1}(L_y/L_x)$ to the x axis and wavelength

$$L_{xy} = \frac{L_xL_y}{L_x^2 + L_y^2}. \tag{4}$$

One option provided is to let the weights increase continuously with spatial wavelength according to $\sqrt{L_{xy}}$. This is equivalent to saying that the longer range structure in the geography of the surface should have a proportionately larger height amplitude. Another option is to choose a weighting function which increases the amplitudes with increasing spatial wavelength for small wavelengths, but which tails off the increase at longer wavelengths. This is provided by a weighting of the approximate form $\sqrt{\tanh(L_{xy}/L_c)}$, where L_c is the wavelength above which the weightings are statistical constant. To see the motivation for this consider a natural crack growing in a section of metal. On a scale of one or two millimetres the crack is able to meander, depending on the local grain structure and imperfections. However, as it gets longer the crack is constrained to lie in the plane of maximum stress so the diversions in direction cannot go on increasing indefinitely with length scale. Figure 12 show a surface generated with the $\sqrt{L_{xy}}$ weighting function current. Studies by Schneider (to be published) based on experimental measurements are giving information on the weighting functions appropriate to natural cracks.

To generate the whole defect's profile using a Fourier series requires over N_xN_y coefficients. In practice this Fourier series can take quite a long time to evaluate at each point[9]. Since the correlation between neighbouring points is imposed by the low spatial frequencies only, while the high spatial frequencies introduce an independence, it seems natural to

[8] Recall that here i is an integer indexing the spectrum of frequencies and not $\sqrt{-1}$.

[9] In the 1980s the speed and memory capacity of personal computers was far less than today, and a concern for program coding.

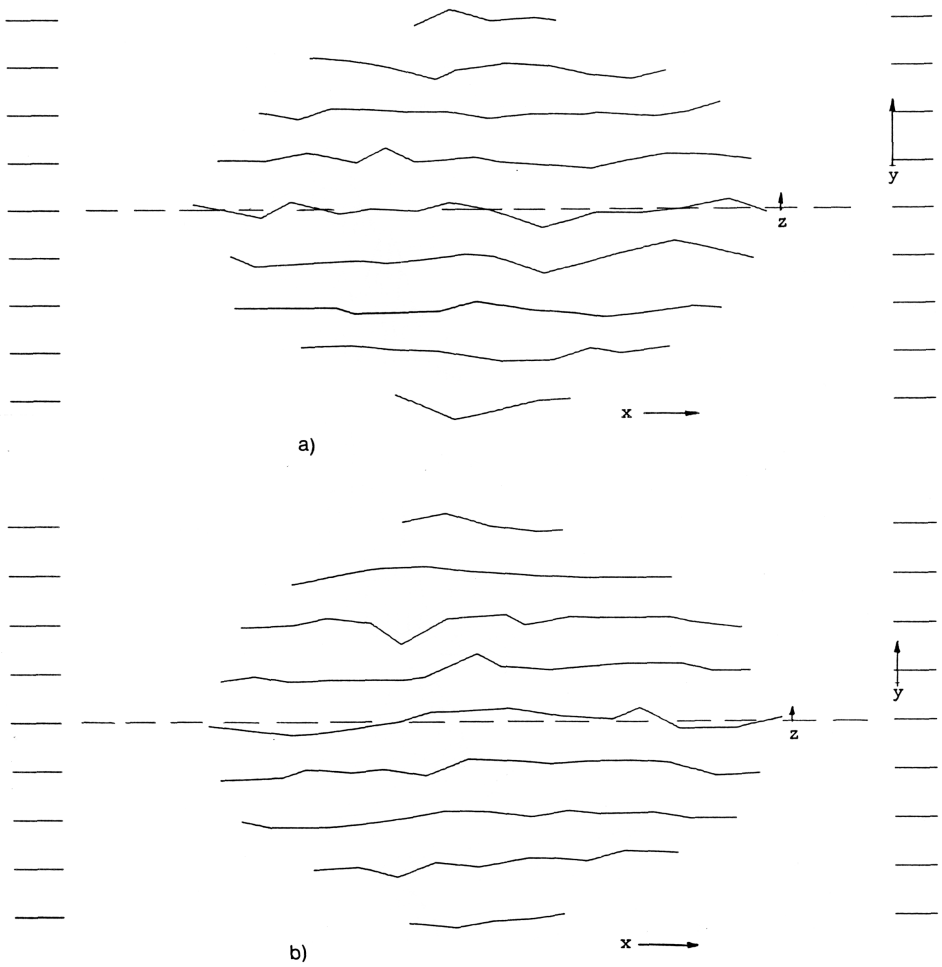

Figure 12: Waterfall plots of two simulated rough defects based on underlying 14×8 distribution of facets in Figure 11. The two realisations are statistically equivalent and were created with the double Fourier series of Eq. 3 using the $\sqrt{L_{xy}}$ weighting function. The values of y correspond to the horizontal lines in Figure 11. The z scale is arbitrary.

save computing time by adopting a hybrid approach to surface simulation. In this a two-dimensional Fourier Series is used but only over the lower frequencies, up to $i = N_x/4$, $j = N_y/4$; an independent Gaussian random number is also generated at each vertex to add a fine tooth to this longer scale geography. This gives a fourfold improvement in computing time. Again one can select whether the weightings of the Fourier coefficients increase progressively with spatial wavelength, or tail off to a constant at longer wavelengths. The relative contributions from low frequency Fourier series and high frequency random numbers determine the quality of the surface structure. Their sum determines the surface roughness.

Appendix E gives calculations relating to the statistics of surface roughness. The program assumes that the mean plane of the surface corresponds closely with the .reference (x, y) plane. Surfaces generated according to Eq 3 can have appreciable tilt from the reference plant, but this can be corrected by subtracting the mean plane as is done for experimentally determined surfaces (see Reference 15).

6 Illustrative applications

The reader will appreciate that the model is sufficiently well developed for it to give useful quantitative guidance on the amplitudes and pulse shapes of signals from rough planar defects in ultrasonic pulse-echo testing. There is clearly enormous scope for carrying out systematic studies of the statistical effects of many parameters on defect response, such as defect size, roughness, angle of incidence, *etc.* At the present stage only a few small numerical simulations have been attempted. These are mentioned in this section to illustrate some of the possibilities of the model. We are naturally cautious about embarking on extensive numerical calculations before the accuracy and range of validity of the model have been more clearly defined by comparison with carefully planned experiments.

6.1 Signal as the probe scans over a defect

One of the most familiar observations of a rough crack in ultrasonic NDT is the A-scan response[10] as the probe scans over the defect, so we take this as a natural starting point for illustrative applications of the model. Figure 13 is a sequence of simulated expanded A-scans as a pulse-echo probe scans over a rough defect at 35° incidence. In this example the defect is 9 mm long in the scan direction by 6 mm wide, has an rms surface height σ of $0 \cdot 16$ mm and lies parallel to the scanning surface. The probe is a 4 MHz, 10 mm diameter 35° shear wave probe (making $\sigma = \lambda/5$) and the mean range to the defect is 50 mm. The details of the example are not important – rather the quite realistic 'travelling echo pattern' is to be noted. This is the Pattern 3 echodynamic of ESI Standard 98-10 and BS 3923 Pt I on ultrasonic weld examination. Observe how the subsidiary peaks move through the pulse envelope as the probe is scanned. The DGS response[11] of a smooth reference reflector of this size at normal incidence is calculated in the program to be 33 dB (on an arbitrary scale), and the calculated peak defect response is $36 \cdot 8$ dB down on this, being therefore equivalent to about $0 \cdot 9$ mm DGS[12].

The little diagrams to the right of the figure illustrate the shifting beam axis in relation to the defect. The axis here is the geometrical axis used in the beam model and does not coincide with the axis measured ultrasonically (unless swept gain is used) except at normal incidence. Because of the fall off in signal with range, the ultrasonic axis in fact leaves the probe at an angle rather less than 35°. This reminds us that the theoretical results should be 'calibrated' for beam angle and index point using a beam plot which is computed by simulating scans over one or more small calibration reflectors. The need for simulating a calibration procedure is another way in which the theory models practical reality.

Another way of looking at echodynamic patterns is simply to plot the peak signal amplitude as a function of probe position. Figure 14 illustrates this. The four graphs are for the same basic 30×5 mm elliptical defect but with different expansions in the height (*i.e.*

[10] The flaw detector screen is calibrated in range and the rectified echo train are displayed in amplitude versus range.

[11] Distance-Gain-Amplitude'. Graphs were published of the theoretical change in amplitude with range of an ideal disc reflector at normal incidence and these were used to compare signals at different ranges.

[12] That is a flat-bottomed hole $0 \cdot 9$ mm diameter.

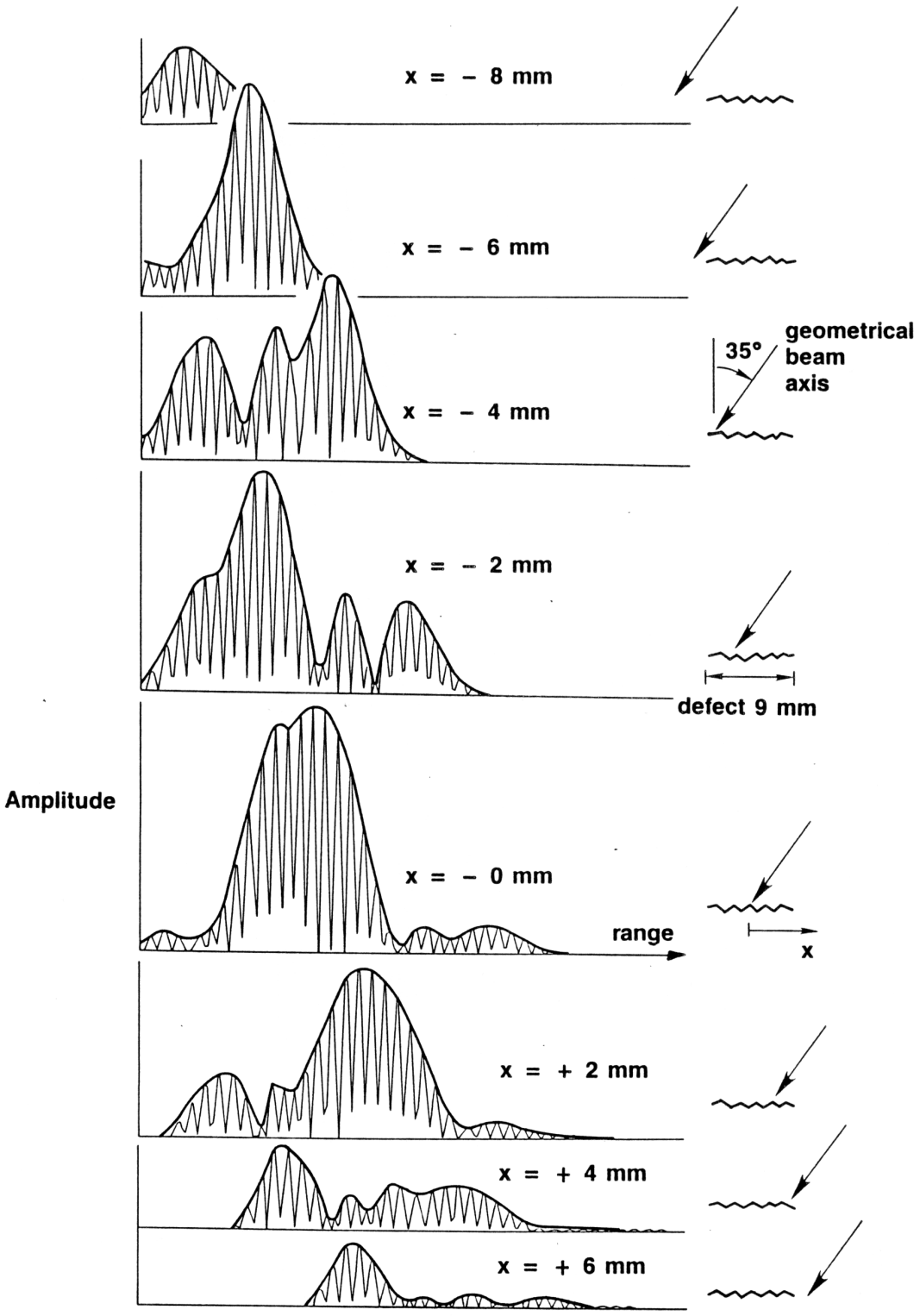

Figure 13: Simulated signal as probe scans over rough defect.

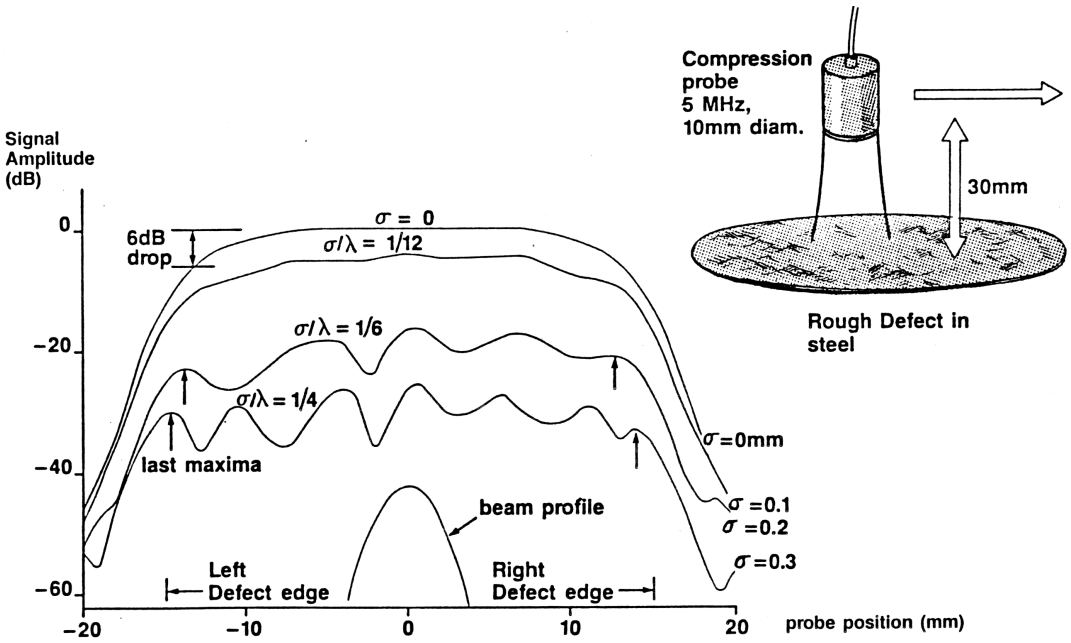

Figure 14: Echo amplitude as a function of probe position along an elliptical defect, 30×5 mm, at normal incidence, for four values of roughness.

roughness). The probe in all four cases was a 5 MHz, 10 nun diameter compression wave probe at normal incidence from 30 mm range, giving a 6 dB beam width at the defect of about 4·5 m. In Figure 14a the defect is perfectly smooth and we see the Pattern 2 echodynamic response of a smooth defect which is longer or wider than the beam width. The 6 dB down points at either end are marked as they would be used in the Half Amplitude sizing technique[13]. In this case they rather underestimate the length of the defect. This is partly because the defect is thin and elliptical and its tips 'fade out' rather than ending abruptly. For curve (b) the rms surface roughness is $0 \cdot 1$ mm, which is about 1/12 wavelength, so the defect is in the intermediate state of roughness where the diffuse scatter is comparable with the coherent. A plateau in response can still be discerned and the Half Amplitude sizing technique is still just about applicable if one drops 6 dB off the values at the two ends of the plateau.

For the other two defect response curves the rms height of the same defect has been scaled up to $0 \cdot 2$ mm, and $0 \cdot 3$ mm respectively. The plateau in response has been broken up by random interference amongst the wavelets scattered from the various facets, and has given way to the more erratically varying Pattern 3a of BS 3923, Pt.l. Clearly at these roughnesses the length of this defect should be estimated ultrasonically using the Maximum Amplitude or 20 dB Drop Techniques. If the 'last subsidiary maxima' at the opposite ends of the defect are identified, one sees that they lie slightly inside the geometrical edges of the defect in this example, which are at ±15 mm. This reminds us of an effect which is recognised from experiments and experience: that the Maximum Amplitude technique, when interpreted strictly, has a small systematic tendency to underestimate defect size, especially near normal incidence. The theoretical model therefore provides a powerful tool for assessing defect sizing

[13] This assumes the beam centre is over the defect's edge when the amplitude has fallen to half its plateau value.

and the errors inherent in the traditional methods. One can readily simulate large numbers of scans across large numbers of defects and so quantify sizing errors statistically. This will be the subject of a future report.

With automated ultrasonic inspection it is usual to obtain C and D scan images of a defect, which are essentially contour plots of defect response over a raster scan, rather than

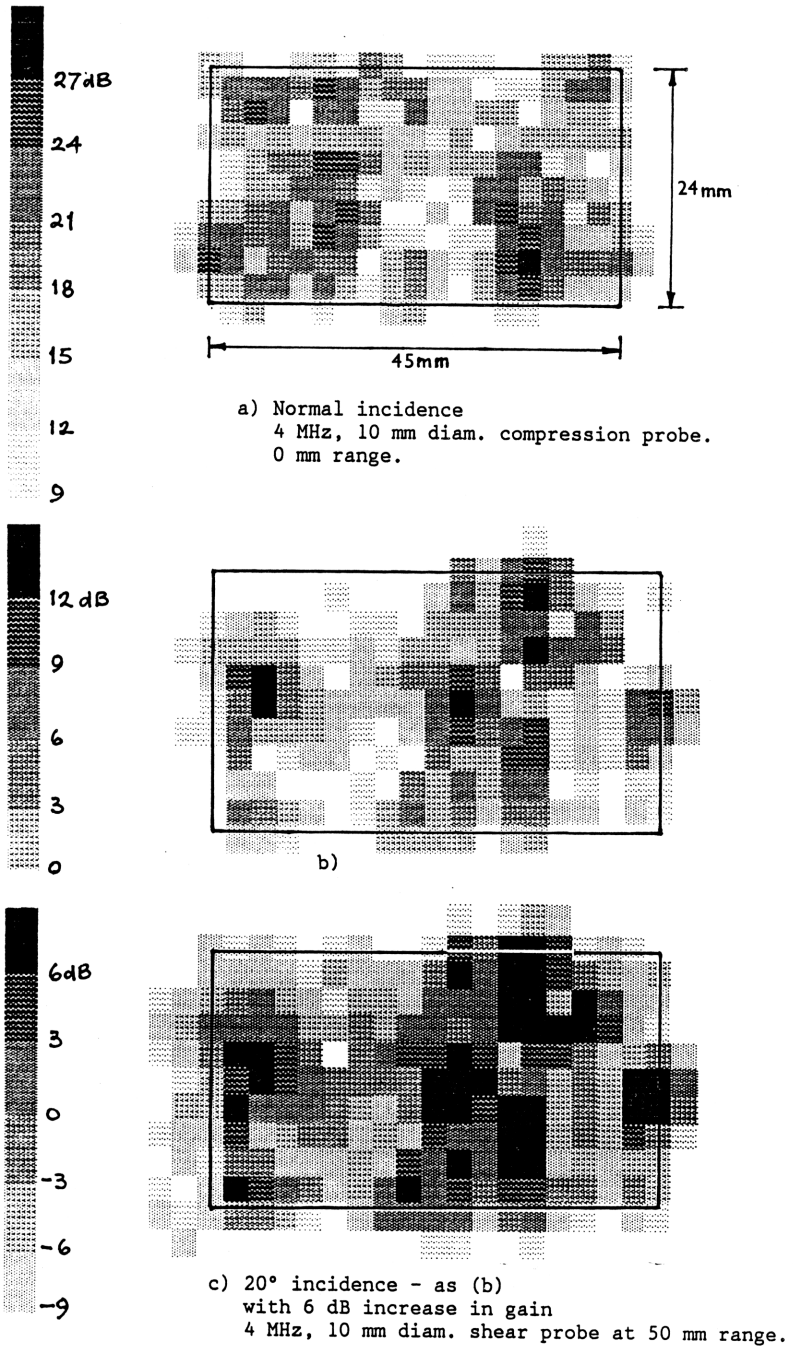

Figure 15: Simulated C-scan displays of 45×24 mm rectangular reflector lying parallel to the scanning surface.

just along a single scan line. Again such displays can be simulated using the model as Figure 15a) to c) illustrate. These are ultrasonic 'plan views' of a 45×24 mm rectangular rough defect, quantised into 3 dB levels as might be done with the DRUID or Micropulse automated equipment[14]. Figure 15a) is for normal incidence with a 4 MHz, 10 mm diameter compression wave probe on steel at 40 mm range. Figure b) and c) are for 20° incidence, with a 4 MHZ, 10 mm diameter shear wave probe on steel at 50 nun range. The sensitivity in c) is 6 dB higher than in b). Again the displays look realistic.

6.2 Effects of increasing roughness

The examples in Figures 14 and 15 have already shown two major effects of increasing roughness – the decrease in pulse-echo signal at normal incidence, and the breaking up of the echodynamic plateau into subsidiary peaks. The decrease in signal with increasing roughness at normal incidence is further illustrated in the graphs of Figure 16. These were obtained as follows. Four approximately circular rough defects, each 8 mm diameter, were simulated by the numerical methods of Section 5. The four surfaces differed in detail but had the same

[14] Early automated ultrasonic equipments in which the probe was scanned in steps by stepper motors and the signals were recorded digitally. Digital technology was just being introduced at the time so most inspections still used analogue instruments.

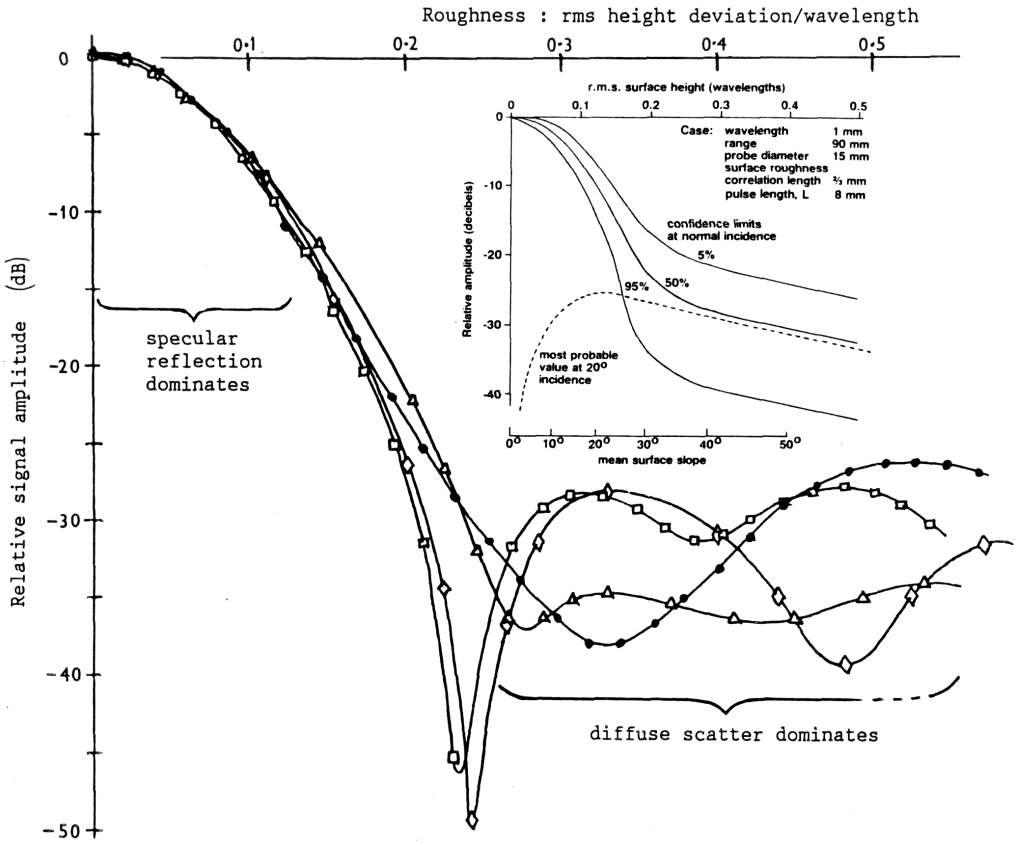

Figure 16: Calculated effect of increasing roughness on amplitude of pulse-echo signal at 0° incidence. Insert is from Coffey. reference 5. $1 \cdot 5$ MHz compression waves in water. Probe 14 mm diam. at 100 mm range.

statistical properties – that is, the parameters of the random number generators were the same for each surface. In the scattering program a 1·5 MHZ, 14 mm diameter 0° compression wave probe in water was simulated at 50 mm (one near-field) range and positioned over the centre of each defect in turn. The back scattered signal was hence calculated and the rms surface height changed by changing the scale factor in the z dimension.

The curves for all four surfaces are virtually identical when the roughness is small, but they increasingly diverge and eventually each meanders erratically. To see the physical reason for this behaviour consider that when the root mean square (rms) surface height is about 1/16 of a wavelength, then the typical peak to valley height is twice this value. At normal incidence the path difference between waves scattered from the peaks and from the valleys in the surface is therefore 1/4 wavelength, allowing for the there-and-back path in pulse echo testing. This is the phase difference that Lord Rayleigh identified as marking the division between constructive and destructive wave interference. Hence, on this simple argument specular reflection completely dominates the diffuse scatter if the rms height deviation of the crack face is less than about 1/16 wavelength. There will be a transition region at about rms = wavelength/8, and at wavelength/4 the wave path differences between peaks and valleys of the surface will be typically one wavelength. At this stage destructive interference is complete and all vestiges of the specular signal are completely lost in the random diffuse scatter.

At the rough limit we are not much interested in the behaviour of any one curve, but rather in the probability of obtaining a signal which is greater than some threshold level when a defect is chosen at random from the whole population of statistically equivalent defects. Moreover, if the probe were allowed to scan over the defects, rather than be fixed exactly over the centre, one would in most cases obtain a somewhat larger signal. In NDT we are probably most interested in the probability distribution of these peak amplitudes. To calculate this requires a simulated raster scan over many defects, and will be presented in a future report.

The insert in Figure 16 is taken from an early paper by the author (ref. 5). It shows the decrease in 5%, 50% and 95% probability limits of signal amplitude at normal incidence as calculated using an analytical expression following Berry (ref. 4). There is strong similarity with the envelope of the numerical results. The insert also shows the predicted change in mean value of signal from the defect's face at oblique incidence based on the analytical expressions. Here the signal grows with roughness. This is because one is observing only the diffuse field, the coherent field having reflected off in the specular direction. To complete the comparison between these early analytical results and the current numerical scattering program, Figure 17 shows the numerically predicted behaviour of peak pulse signal amplitude at 20° incidence for the same four surfaces studied in Figure 16. In the numerical simulation the signals for small roughness arise by diffraction at the defect edges only and are well resolved in range. Edge waves were not included in the insert in Figure 16, which largely explains the smaller amplitudes in the early analytical results. Note also that at oblique incidence the signals received in different azimuths, at the same polar angle of incidence, are essentially independent. Figure 17 includes graphs for two azimuths of the incident beam – 0°/180° and 90°/270° – for one of the surfaces.

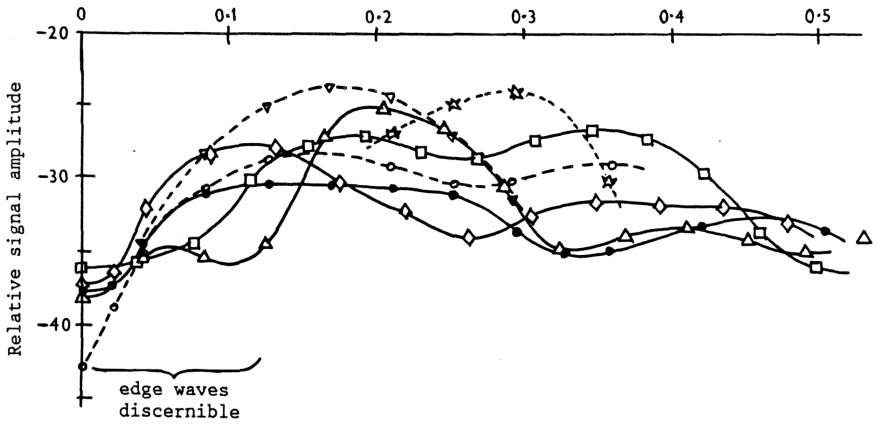

Figure 17: As Figure 16 but at 20° incidence.

6.3 Effects of angle of incidence and range

To further illustrate the effect of angle of incidence on defect response in back-scatter, Figure 18 has been calculated for two of the same defects at a roughness whose rms height is $0 \cdot 1$ mm and for the same $1 \cdot 5$ MHz, 14 mm diameter compression wave probe in water ($\sigma = \lambda/l0$). Also shown in the figure is the behaviour which would be expected were the defect perfectly smooth. Although interference causes much oscillation in response for the rough defects, we see that the graphs on average look like the sum of two components - a strong narrowly peaked, specular, coherent component, and a much weaker, broader diffuse component. The bands marked by the dashed lines indicate approximately the average behaviour of the random diffuse scatter. The meanderings of the diffuse signal are exaggerated here because the calculation was carried out for continuous waves rather than the pulse option used in Figure 17.

The final illustrative example is in Figure 19, which shows graphs of the effects of increasing range on the signal from rough circular defects at normal incidence. When the defect is at sufficient range that it is smaller than the beam width, the signal falls at $1/R^2$ as we would expect. For a larger defect, however, increasing range means that more of the surface is being illuminated by the expanding beam and these extra facets modulate the signal, depending on whether the wavelets they contribute add in or out of phase. Consequently, there is no simple range behaviour of any individual large rough surface, though on *average* they will behave like a large, smooth but attenuating reflector at normal incidence.

6.4 Applications to other questions in ultrasonic NDT

The main theoretical idea in this report is to split the Kirchhoff integral (by which the ultrasonic signal at a distant point is calculated) into two types of part : i) analytical integration over small triangular elements taken one at a time, and ii) numerical summation of the contributions of all these elements. Though this scheme was devised to deal with rough, facetted reflectors, it is in principle equally applicable to all scattering and sound radiation problems in ultrasonics which can be represented as a surface integral of Huygens' sources. For instance, one such area of ultrasonic NDT is the design of ultrasonic probes, where radiation from the crystal is represented as an integral. The effects of intermediate interfaces, such as the cou-

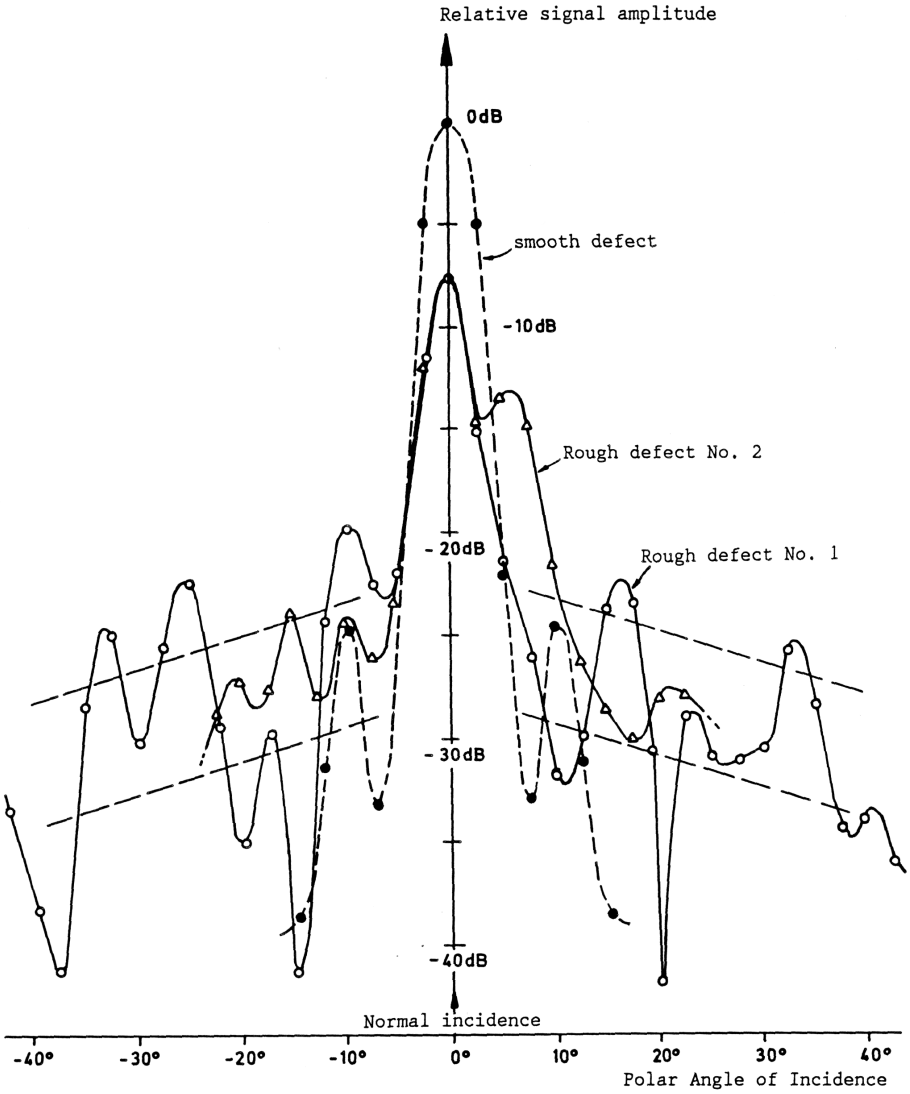

Figure 18: Calculated variation in pulse-echo signal with angle of incidence on 8 mm diameter reflectors. Rough reflectors have $\sigma = \lambda/10$. Case of $1 \cdot 5$ MHz compression waves in water. 14 mm diam. probe, 1000 mm range.

pling layer under the probe, can also in principle be described by a wave integral over the area of the probe shoe. Some preliminary application of this approach to the lens effects under a probe on an uneven surface has already been made at the NDTA Centre.

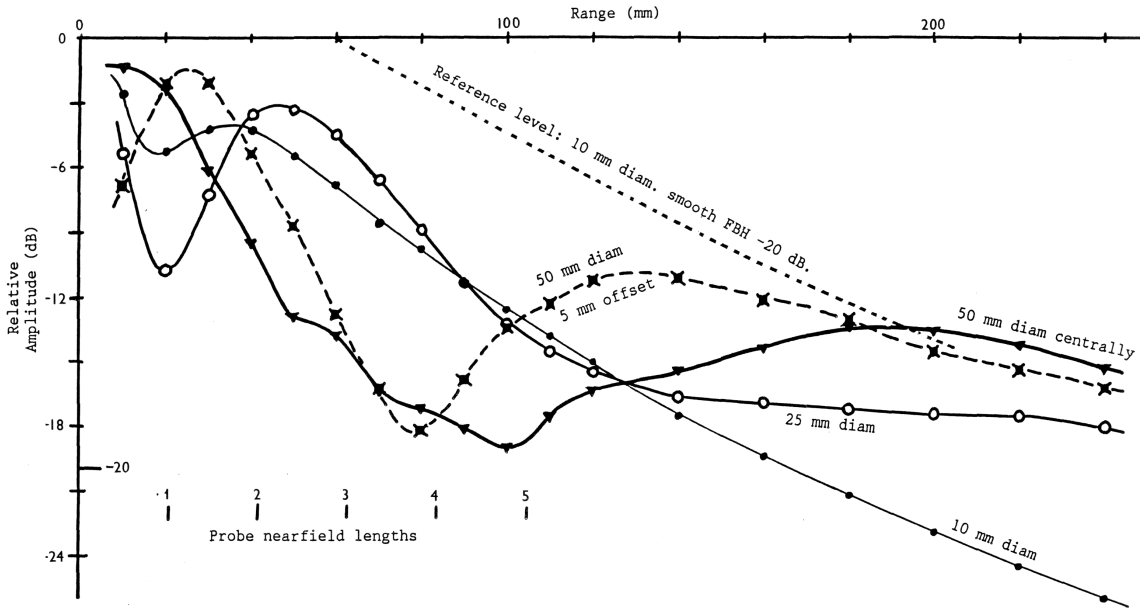

Figure 19: Variation in signal amplitude with range for various sizes of rough planar reflector at normal incidence. Examples for case of defect 10, 25 and 50 mm diameter with $\sigma = 0 \cdot 3$ mm and 5 MHz, 0° compression wave probe in steel ($\lambda = 1 \cdot 19$ mm, nearfield length 21 mm). The range at which the incident beam has fallen by 20 dB at the edges of the 25 mm and 50 mm defects are respectively 100 and 200 mm. For the 50 mm defect one curve is with the probe positioned centrally, and the other with a 5mm displacement from centre.

7 Conclusions

1. An approximate mathematical model to predict the ultrasonic pulses detected from rough cracks has been developed. A computer program has been written to deal with the pulse-echo mode of inspection. All the essential features of the ultrasonic inspection, including the probe type and the defect's size, position, orientation and roughness, are included in the program.

2. Despite some fundamental limitations in the mathematics, the model gives predictions which appear plausible and realistic. Moreover, relevant to defect sizing, there are statistical arguments for believing that the shapes of the predicted echodynamic patterns are broadly correct. Therefore the model is likely to be of significant practical benefit in helping predict the ultrasonic detectability of rough cracks, and the errors in defect size measurement.

8 Recommendations

1. The model should be verified by comparison with experimental evidence. In the first instance this should involve comparison of the model's predictions with currently available data. Where shortcomings in the experimental data are identified, consideration should be given to a specific programme of experimental verification.

2. In order to allow the model to be applied to actual natural rough cracks, it should

be interfaced with the crack surface profile measurements of Franklin, Schneider and Webster (CEGB Report OED/STN/87/20151/R).

9 Acknowledgements

I am most grateful to Susan Franklin for her assistance in producing some of the computer-generated plots in Section 6. The program described has been translated into FORTRAN by Dr. R. K. Chapman, who also made useful comments on the manuscript. Mr. C. Schneider gave useful advice on the statistics of rough surfaces.

10 References

1. Coffey, J.M. ,"Mathematica1 modelling - what it is and what it does". Proc. Conf. on 'Mathematical Modelling in NOT'. Cambridge 2/3rd Sept, 1986. Published Inst. Maths & Applicns. Also CEGB Report No. OED/STN/87/20138, May 1987.

2. Chapman, R.K. "An integrated model of ultrasonic NDT and its practical application". Proc. Conf. on Mathematical Modelling in NDT". (see ref.l). Also CEGB Report No. OED/STN/87/20102. March 1987 (See also ref. 11 and 12).

3. Ogilvy, J.A. "A review of literature on wave scattering from rough surfaces". UKAEA Report AERE R 12337., June 1986. Also to be published in Reports in Progress in Physics. Vol. 50, Dec. 1987.

4. Berry, M.V. "The statistical properties of echoes diffracted froiii rough surfaces". Proc. Roy. Soc. Vol 273A 611-654, (1973).

5. Coffey, J.M. "Quantitative Assessment of the Reliability of Ultrasonics for Detecting and Measuring Defects in Thick-Section Welds". Paper in Proc. Conf. on "Tolerance of Flaws in Pressurised Components". London 16th-l8th May, 1978. Publ. I. Mech. Eng.

6. Coffey, J.M., Franklin, S.P. and Schneider, C.R.A. "Rough Crack-like Defects - Surface Morphology and Ultrasonic Scattering". Proc. 4th Europ. Conf. on NOT, Sept. 14-18, London 1987 Publ. Pergamon.

7. Toft, M.W. "Experimental Studies of Ultrasonic Reflection from Various Types of Mis-oriented Defect". Proc. 2lst Annual Conf. Brit. Inst. NOT. Newcastle-upon-Tyne, Sept. 1986. Publ. EMAS.Also CEGB Report OED/STN/87/20060/R.

8. Ogilvy, J.A. "Computer simulation of acoustic wave scattering from rough surfaces". UKAEA Report AERE-TP.1235. Also to be published in J. Phys. D.

9. Haines, N.F. and Langston, D.R. "The reflection of ultrasonic pulses from surfaces". J. Acoust. Soc. Amer. Vol 67 NO.5, 1443-1454. May (1980). Also CEGB Report RD/B/N4115 Sept. 1977.

10. a) Born, M. and Wolf, E. "Principles of Optics". Publ. Pergamon. Fifth Edn. 1975 pp 375 et seq.

b) Longhurst, R.S. "Geometrical and Physical Optics". Publ. Longmans. 2nd Edn. 1967. pp. 200-203.

11. Coffey, J.M. and Chapman, R.K. "Application of elastic scattering theory for smooth flat cracks to the quantitative prediction of ultrasonic defect detection and sizing". J. Nucl. Eng. Soc. Vol 22. p319-333 Oct.(l983)

12. Chapman, R.K. "Ultrasonic Scattering from Smooth Flat Cracks - An elastodynamic Kirchhoff diffraction theory (main report). CEGB Report NWR/SSD/84/0059/R. Sept 1984.

13. Wagner, R.J. "Shadowing of Randomly Rough Surfaces". J. Acoust. Soc. Amer. Vol 41. 138-147 (1967).

14. Chapman, R.K. and Toft, M. Theoretical prediction and experimental verification of time dependent ultrasonic response of smooth defects". Proc. 4th Euro. Conf. on NOT, London Sept. 1987, Publ. Pergamon. Also CEGB Report. No. OED/STN/87/20199/R.

15. Franklin, S.P., Schneider, C.R.A. and Webster, P. "An Instrument for measuring the Surface Height Contours of Rough Crack Faces". CEGB Report OED/STN/87/20101/R June 1987

Appendix A: Transformation from defect to facet co-ordinates

The defect and probe are specified to the program by the user in the (x, y, z) co-ordinate system, with origin O at the centre of the defect (Figure 1). The Kirchhoff scattering calculation is carried out for each facet in a local co-ordinate system (u, v, w), Figure 2. This appendix derives the geometrical transformation from the first system to the second.

Figure Al shows both co-ordinate systems in relation to one chosen facet. We will call the position vectors of the three corners of the triangle $\mathbf{P_1} = (P_{1x}, P_{1y}, P_{1z})$, $\mathbf{P_2}$ and $\mathbf{P_3}$, in the global (x, y, z) system, and $\mathbf{A_1} = (A_{1u}, A_{1v}, A_{1w})$, $\mathbf{A_2}$ and $\mathbf{A_3}$ in the local (u, v, w) system. The centroid of the triangle is $\mathbf{C} = (\mathbf{P_1} + \mathbf{P_2} + \mathbf{P_3})/3$ in the (x, y, z) system, and it defines the origin of the (u, v, w). The w axis is normal to the facet so the vector cross product of any two edges of the triangle will be parallel to $\mathbf{e_w}$, where $\mathbf{e_w}$, is a unit vector in the w direction. Thus

$$\mathbf{e_z} = \frac{(\mathbf{P_2} - \mathbf{P_1}) \times (\mathbf{P_3} - \mathbf{P_1})}{M_z}$$

where M_z is the modulus of the numerator. Note, in passing, that the identity

$$(\mathbf{P_2} - \mathbf{P_1}) \times (\mathbf{P_3} - \mathbf{P_1}) = (\mathbf{P_1} \times \mathbf{P_2}) + (\mathbf{P_2} \times \mathbf{P_3}) + (\mathbf{P_3} \times \mathbf{P_1})$$

gives an alternative way for computing $\mathbf{e_z}$.

The v axis is also readily found as being in the direction from centroid to vertex P_3. The unit vector is

$$\mathbf{e_v} = \frac{1}{M_v}\left[\mathbf{P_3} - \tfrac{1}{3}(\mathbf{P_1} + \mathbf{P_2} + \mathbf{P_3})\right],$$

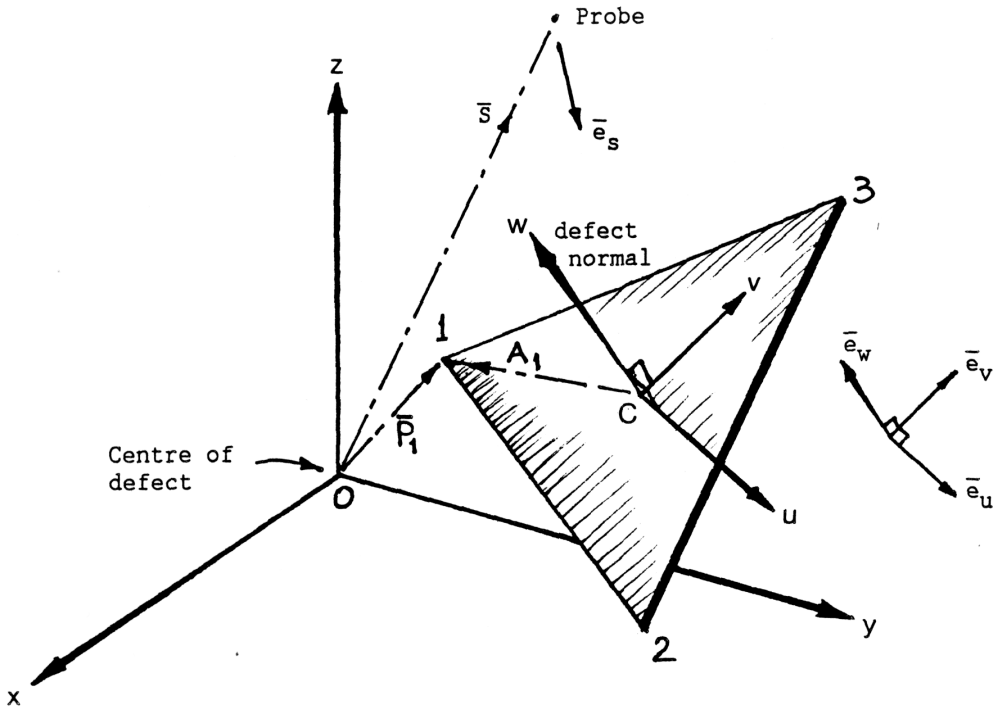

Figure A1 : Defect and facet co-ordinate systems.

M_v being the modulus of the numerator. Note that this line through centroid and P_3 bisects the side P_1P_2; $\mathbf{e_v}$ is parallel to

$$\mathbf{P_3} - \tfrac{1}{2}(\mathbf{P_1} + \mathbf{P_2}).$$

The u axis is mutually perpendicular to the w and v axes, so

$$\mathbf{e_u} = \mathbf{e_v} \times \mathbf{e_w}.$$

Any vector $\mathbf{P}$ in the (x, y, z) frame can be expressed as a vector $\mathbf{A}$ in the (u, v, w) frame by the matrix equation

$$\mathbf{A} = \mathcal{T}(\mathbf{P} - \mathbf{C}) \qquad \text{or}$$

$$\begin{pmatrix} A_u \\ A_v \\ A_z \end{pmatrix} = \begin{pmatrix} \mathbf{e_u} \cdot \mathbf{e_x} & \mathbf{e_u} \cdot \mathbf{e_y} & \mathbf{e_u} \cdot \mathbf{e_z} \\ \mathbf{e_v} \cdot \mathbf{e_x} & \mathbf{e_v} \cdot \mathbf{e_y} & \mathbf{e_v} \cdot \mathbf{e_z} \\ \mathbf{e_w} \cdot \mathbf{e_x} & \mathbf{e_w} \cdot \mathbf{e_y} & \mathbf{e_w} \cdot \mathbf{e_z} \end{pmatrix} \begin{pmatrix} \mathbf{P_x} - \mathbf{C_x} \\ \mathbf{P_y} - \mathbf{C_y} \\ \mathbf{P_z} - \mathbf{C_z} \end{pmatrix}.$$

The matrix $\mathcal{T}$ describes a rotation in three-dimensions about the centroid. From this the co-ordinates A_{1u}, A_{1y}, *etc.* of the vertices of the triangle are readily calculated. Through there are 9 co-ordinates, three for each vertex, only four are non-trivial when expressed in the (u, v, w) frame. All the w components are zero by intent. Also $A_{3u} = 0$ and $A_{1u} = -A_{2u}$. Furthermore $(A_{1y} + A_{2y}) = -A_{3y}$.

Finally denote the probe's position in the (x, y, z) frame by $\mathbf{S}$. Then a unit vector $\mathbf{e_s}$ pointing from the probe to the centroid of the facet is

$$\mathbf{e_s} = \frac{1}{R_0}\mathcal{T}(\mathbf{S} - \mathbf{C})$$

where $\mathcal{T}$ is the transformation matrix above and R_0 is the modulus of $(\mathbf{S} - \mathbf{C})$, which is the range to that facet. Note that $\mathbf{e_s}$ does *not* necessarily correspond to the beam axis; in general, an off axis ray will strike any arbitrary facet.

Appendix B: Scattering from a triangular facet in the acoustic Kirchhoff approximation

This appendix derives the formulae for back scattering of time harmonic scattering of scalar waves from an isolated, independent triangular reflector in the Kirchhoff approximation. These formulae are central to the triangular facet model[15].

B1 The Kirchhoff scattering formula

The fundamental Kirchhoff formula, giving the wave field ψ at any point P_0 caused by scattering of an incident wave ψ_{inc} from a reflector Δ, is derived in most standard texts on optics such as those cited in reference 10, and so it will not be elaborated upon here. The result for a hard reflector is

$$\psi P_0) \;=\; \frac{1}{\lambda} \iint_{\Delta} \psi_{inc}(\Delta)\, \frac{e^{ikr}}{R}\, (\mathbf{e_R} \cdot \mathbf{n})\, d\Delta \qquad (b1)$$

where λ is the wavelength, k the wave number $= 2\pi/\lambda$, R the range from P_0 to a general point on Δ, $\mathbf{e_R}$ a unit vector along R from P_0. The vector dot product $\mathbf{e_R} \cdot \mathbf{n}$ is called the 'obliquity factor' and is just the cosine of the angle between normal and scattered ray. It means that the signal is determined in part by the projected area of the defect along the scattered ray direction. If $\mathbf{e_R} \cdot \mathbf{n}$ is negative it means that one is trying to illuminate from its underside, which is not possible. Therefore $\psi_(P_0)$ is set to zero in such cases. (See Appendix D on shadowing in this context.)

The formula (bl) above applies only at a receiving point and it is necessary to take into account that the probe has a finite area over which it integrates the detected wave field. A pulse-echo probe will also determine the sound field, ψ_{inc}, incident on the defect. References 11 and 12 discuss how the Reciprocity Theorem of physics requires that the response of a probe acting in reception to a unit point source at arbitrary position Q, is proportional to the field which would be produced at Q when the probe transmits under unit stimulus. This is dealt with mathematically by replacing the spherical wave $\exp(ikR)/\lambda R$ with the probe's field, ψ_{inc}. ψ_{inc} will be calculated using the beam model of Appendix C. We can also equate the unit vector $\mathbf{e_R}$ along the scattered ray with the incident unit vector, $\mathbf{e_s}$, from the source of sound, introduced in Appendix A and shown in Figure A1.

The incident field varies over the facet as the notation $\psi_{inc}(\Delta)$ implies. It will be fairly clear that the amplitude will not vary much, especially if the facet is small. However the range R to various points may change appreciably in relation to the wavelength, and so give rise to significant destructive interference. This interference, together with the incident field and the projected area of the facet, essentially determine the received signal strength. The range to any particular point on the reflector R can conveniently be split into $R_0 + \delta R$ where R_0 is the range to the centroid of the facet and δR the small difference. Since the probe is functioning in pulse echo, the path difference is twice the range difference. Taking these thoughts together,

[15] A parallel derivation of these formulae is given in my article on sound radiation on *www.mathstudio.co.uk*.

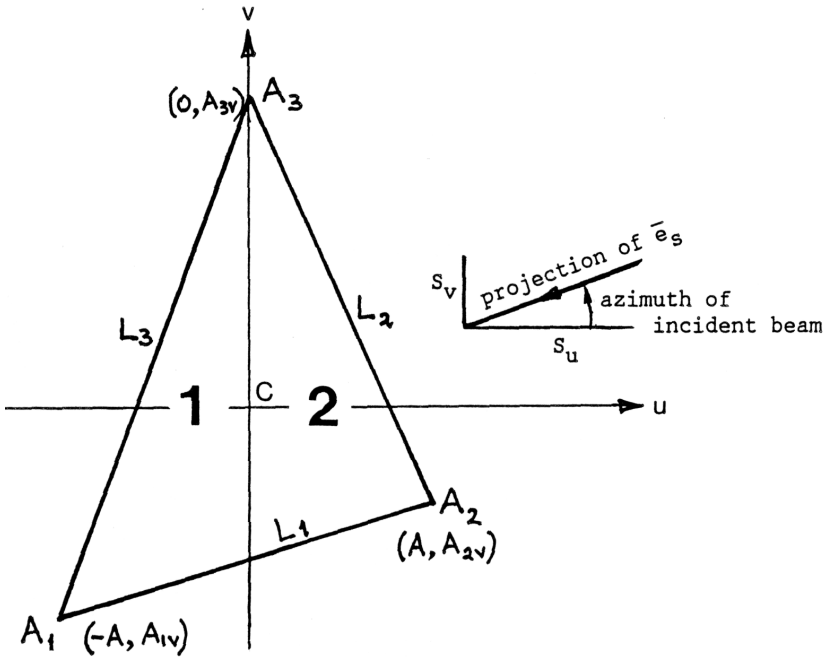

Figure B1 : Notation for calculating Kirchhoff integral over triangle.

expression (bl) becomes modified to

$$\text{Signal at } P_0 \;\propto\; \psi^2_{inc}(C)\,[\mathbf{e_S}(C)\cdot\mathbf{n}]\iint_\Delta \exp(2ik\,\delta R)\,d\Delta, \tag{b2}$$

where C denotes the value at the centroid. $[\mathbf{e_S}(C)\cdot\mathbf{n}]$ is the obliquity factor.

It only remains to find δR in order to have a working formula for evaluation. Let $\mathbf{q}$ be the position vector of an arbitrary point Q on the reflector's surface, measured from the centroid C. Then

$$\delta R \;=\; \mathbf{q}\cdot\mathbf{e_s}, \tag{b3}$$

which is the projection of $\mathbf{q}$ along the incident ray. δR can be either positive or negative depending on the position of Q and the tilt of the reflector. If the components of $\mathbf{q}$ in the 'facet' co-ordinate system (Appendix A) are (u, v, w) and of $\mathbf{e_s}$ are (S_u, S_v, S_w), calculation of the received signal from a single facet amounts to evaluating the integral, I, of

$$\exp\{2ik[uS_u + vS_v]\}.du\,dv \tag{b4}$$

over the triangle.

B2 Evaluation of the integral in the general case

The triangle is shown again in Figure Bl. Its sides are the lines L_1, L_2, L_3, and these define the limits of integration. The integration is performed by splitting the triangle into its left and right hand sub-triangles, labelled 1 and 2 in Figure Bl. We note again that $A_{1u} = -A_{2u} = A$, say, and use this to write the lower limit as

$$L_1 \;=\; m_1(u + A) + A_{1v} \quad \text{where } m_1 \;=\; \frac{1}{2A}(A_{2v} - A_{1v})$$

$$L_1 = m_1(u - A) + A_{2v}$$

and similarly for the upper limits L_3 and L_2:

$$L_3 = m_3(u + A) + A_{1v} \quad \text{where } m_3 = \frac{1}{A}(A_{3v} - A_{1v})$$

$$L_2 = m_2(u - A) + A_{2v} \quad \text{where } m_2 = -\frac{1}{A}(A_{3v} - A_{2v}) \qquad (b5)$$

The signal is therefore proportional to $I = I_1 + I_2$ where

$$I_1 = \int_{-A}^{0} du \int_{L_1}^{L_2} dv . \exp\{2ik[uS_u + vS_v]\} \qquad (b6)$$

$$I_2 = \int_{0}^{A} du \int_{L_1}^{L_2} dv . \exp\{2ik[uS_u + vS_v]\} \qquad (b7)$$

The integration over v is readily performed, and substitution of the limits L_2 and L_3 leads to I_1 as a sum of two subsidiary integrals over u, I_{1a} and I_{1b} respectively;

$$I_{1a} = \frac{-i}{2kS_v} \exp\{2ikS_v[A_{1v} + m_3 A]\} \int_{-A}^{0} \exp\{2ik[S_u + m_3 S_v]u\} . du$$

and similarly for I_{1b}. The integral over sub-triangle number 2 is treated in the same way and one obtains the final integral over the triangular facet as the sum $I_{1a} + I_{1b} + I_{2a} + I_{2b}$ where

$$I_{1a} = \frac{+g(S_v A_{1v})}{h(m_3)} \{g(-S_u A) - g(m_3 S_v A)\}$$

$$I_{1b} = \frac{-g(S_v A_{1v})}{h(m_1)} \{g(-S_u A) - g(m_1 S_v A)\}$$

$$I_{2a} = \frac{-g(S_v A_{2v})}{h(m_2)} \{g(S_u A) - g(-m_2 S_v A)\}$$

$$I_{2b} = \frac{+g(S_v A_{2v})}{h(m_1)} \{g(S_u A) - g(-m_1 S_v A)\}$$

$$\text{where} \quad g(z) = \exp[2ikz] \qquad (b8)$$

$$\text{and} \quad h(m) = 4k^2 S_v[S_u + mS_v].$$

This is the required general result, giving the detected signal through equation (b3).

B3 Special cases

The Kirchhoff integral, involving the sum of I_{1a} *etc.* in (b8), requires special consideration to find its value when any of the denominators $h(m_{1,2,3})$ is zero. We can distinguish five special cases:

a) $S_u = S_v = 0$, corresponding to normal incidence,

b) $S_v = 0$, corresponding to the incidence beam in the (uw) plane,

c) $S_u = -m_1 S_v$, corresponding to incidence squarely n the side L_1,

d) $S_u = -m_2 S_v$, incidence normal to L_2,

e) $S_u = -m_3 S_v$, incidence normal to L_3.

The limiting values of the integral $I = I_1 + I_2$ can readily be found by expanding the exponentials in $g(z)$ as the first one or two terms of a power series and looking for cancellations and common factors. For instance, taking case b, at $S_v = 0$,

$$I_1 \;=\; \frac{[1 - \exp(-2ikS_uA) - 2ikS_uA](m_3 - m_1)}{4k^2 S_u^2}$$

$$I_2 \;=\; \frac{[1 - \exp(+2ikS_uA) + 2ikS_uA](m_1 - m_2)}{4k^2 S_u^2}$$

If substitution is made for $m_{1,2,3}$ from equations b5, one finds the combination of terms

$$A_{3v} - \tfrac{1}{2}A_{1v} - \tfrac{1}{2}A_{2v}$$

appearing, which is the height of the triangle up the v axis; when multiplied by A it gives the area Δ of the triangle. The result for $I = I_1 + I_2$ at $S_v = 0$ is

$$\frac{2\Delta(1 - \cos(2kS_uA))}{(2kS_uA)^2}. \qquad (b9)$$

The behaviour for normal incidence is a more particular case of this, and is readily found by expanding the cosine function for small argument and letting S_u tend to zero:

$$I(0^\circ \text{ incidence}) \;=\; A(A_{3v} + \tfrac{1}{2}|A_{1v} + A_{2v}|) \;=\; \Delta. \qquad (b10)$$

In other words, the integral is here just the area of the triangle, as we would expect.

To deal with the cases of normal incidence on an edge of the triangle, one sets $S_v m_j = -S_u + \varepsilon$ where ε is small, and proceeds to expand the exponentials. The results for cases c), d) and e) are respectively:

Case c): $I_{1b} + I_{2b}$ becomes

$$\frac{g(S_vA_{2v})[g(S_uA) - g(S_vA)] \;-\; g(-S_vA_{1v})[g(-S_uA) - g(-S_vA)]}{4k^2\, S_v(S_u - S_v)}$$

Case d): I_{2a} becomes

$$\frac{-ia}{2kS_v}\, g(+S_uA + S_vA_{2v}) \qquad (b11)$$

Case e): I_{1a} becomes

$$\frac{-ia}{2kS_v}\, g(-S_uA + S_vA_{1v})$$

B4 Graphs of the Kirchhoff integral

Figures B2 and B3 show graphs of the amplitude and phase of the the Kirchhoff integral I for an equilateral triangle.

In Figure B2 the sides are two units long, the wavelength is one unit. Graphs are given of the dependences on polar angle of incidence for incident azimuths of 0°, 15° and 30°. Because of the high symmetry of the equilateral triangle, the window from 0° to 30° contains all distinct azimuths. The top panel shows the phase variation for angles of incidence from normal to grazing. When the beam lies in a plane containing an edge (*i.e.* 0° azimuth), the phase is zero for all angles of incidence, as equation (b9) requires. The corresponding amplitudes of I are shown in Figure B2(b). Also plotted is the obliquity factor, $\mathbf{e_s} \cdot \mathbf{n}$. The received signal is proportional to $I\,\mathbf{e_s} \cdot \mathbf{n}$ and hence is always zero at grazing incidence (90°) even though I itself is generally non-zero at 90°.

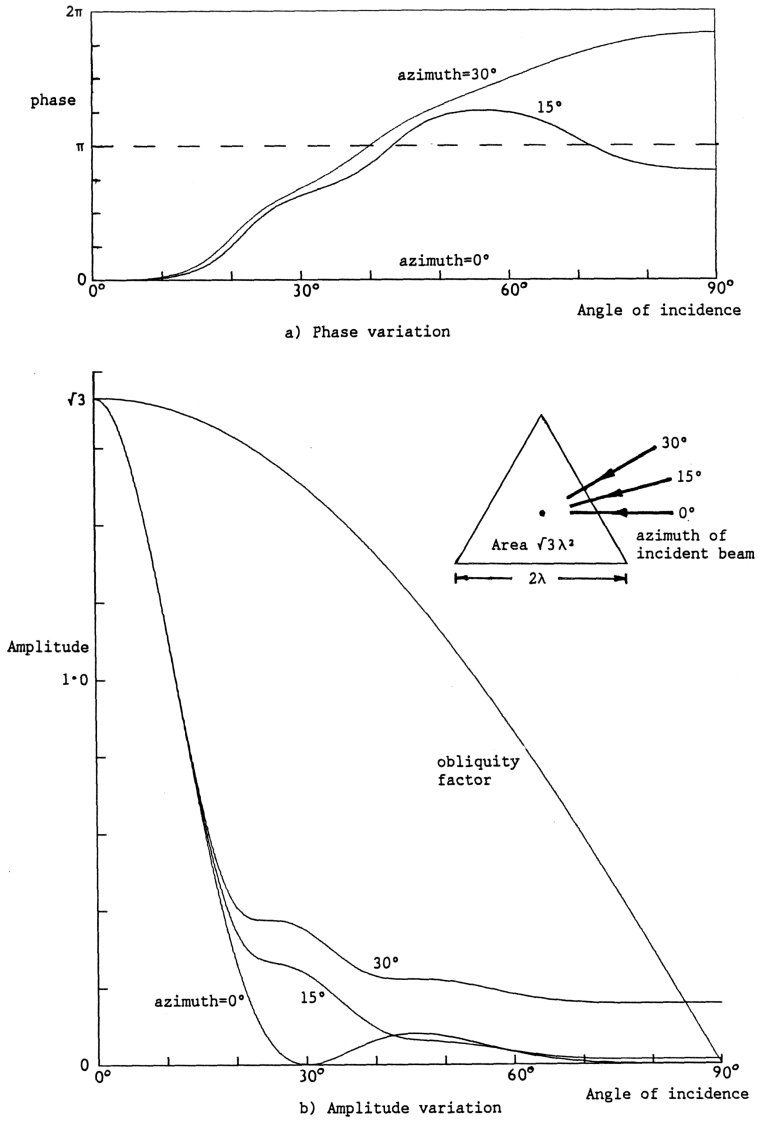

Figure B2: Kirchhoff integral, Eq b8, for back scatter from an equilateral triangle, side 2λ..

Figure B3 gives equivalent graphs of the amplitude and phase of integral I as functions of the angle of incidence for an equilateral triangle of side one unit. (a) and (c) are the phase and amplitude respectively when the wavelength is 1 unit, and (b) and (d) are for a wavelength of $\frac{1}{2}$ unit. First note that the amplitude at normal incidence is one quarter of that in Figure B2 since the area of the triangle has been reduced by $\frac{1}{4}$ as equation (b10) requires. A second point is that for the $\lambda = \frac{1}{2}$ cases, (b) and (d), the horizontal scale has been expanded by a factor of two. This is to emphasise that, to a good approximation, when the wavelength decreases, the width of the 'polar diagram' of the defect becomes proportionately narrower. The amplitude and phase plots for $\lambda = 1$ and $\frac{1}{2}$ are virtually identical, apart from this scaling, to angles well beyond the main lobe in response.

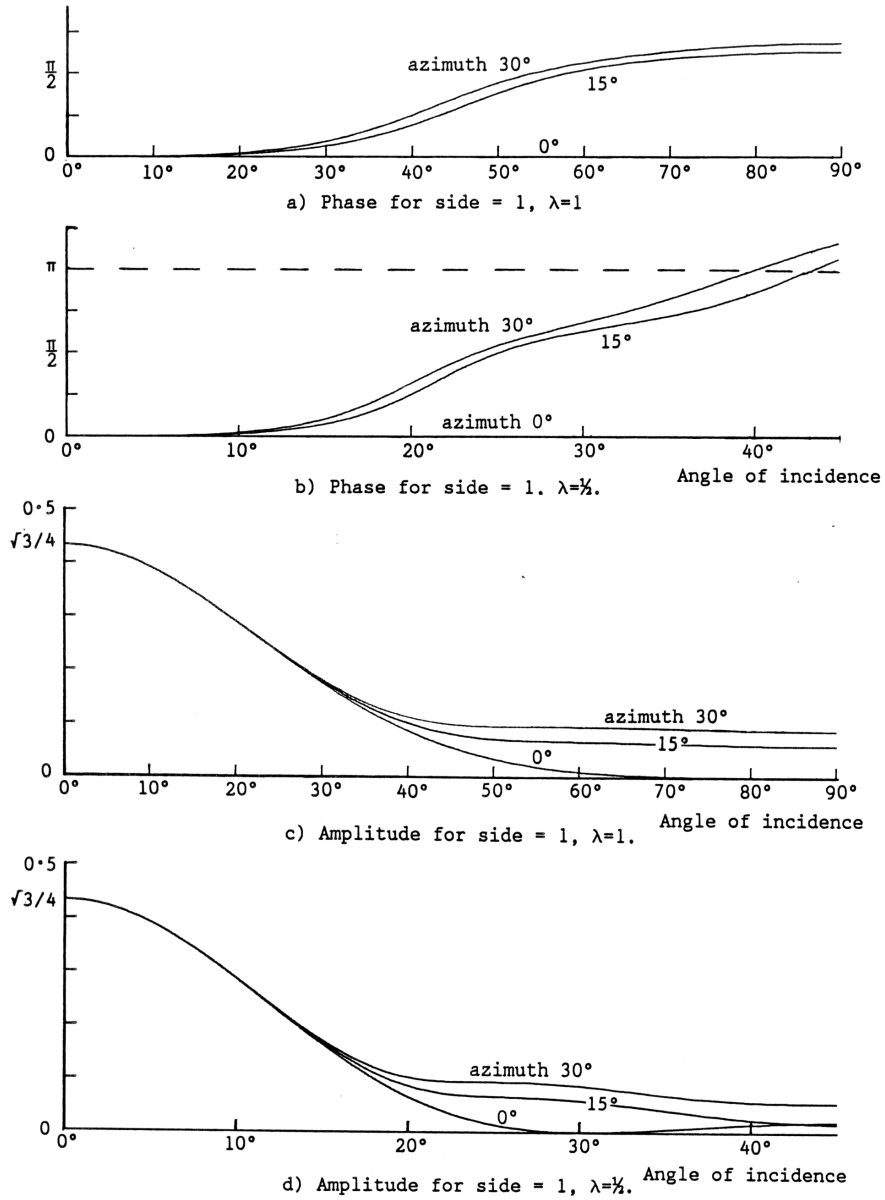

Figure B3: Comparison of amplitudes and phases of Kirchhoff integral, Eq b8, for an equilateral trriangle when wavelengthy changes by factor of 2.

Appendix C: Model of the ultrasonic beam, and signals for a FBH reference reflector

C1 Beam Model

The author devised an analytical expression which gives approximately the complex wave field radiated from a probe at ranges beyond about 0·8 nearfield lengths. The derivation is outlined in References ll and 12. Briefly, we note that the far field radiated from a circular crystal varies with angle θ away from the beam axis as $J_1(q)/q$ where $q = kc\sin\theta$, c being the crystal radius and $J_1(q)$ the first order Bessel function. The simpler function $(1-q^2/15)\exp(-q^2/15)$ closely approximates to $2J_1(q)/q$. It is not difficult to apply the Fourier-Bessel transform and find that the amplitude distribution over the probe face which gives the exact far field $(1-\zeta)e^{-\xi}$, $\zeta = q^2/15$ is

$$\eta^2 \exp\left(-\frac{4\eta^2}{15}\right), \qquad \eta = \frac{15r}{4c} \tag{C1}$$

where r is the radial distance out from the centre of the crystal. Expression (Cl) can be evaluated in the Fresnel approximation to determine the field that would be radiated from a probe where amplitude across the crystal face is that given by (Cl). The result is;-

$$\psi(R,\rho) = -i\pi\frac{N}{R}\exp(ikR)\,\frac{1}{B^2}\,(1-A_\rho)\exp(-A_\rho), \tag{C2}$$

$$B = 1 - \frac{i4\pi N}{15R}$$

where R is the distance from the centre of the crystal to the point of observation, ρ is the lateral distance to this point measured perpendicular to the beam axis, $A_\rho = (\nu c)^2/15B$ where $\nu = k\rho/R$, k is the wave number and N is the nearfield length $= c^2/\lambda$. This is the equation of the beam model used in the scattering program. Reference 11 describes its generalisation to elliptical, rectangular and focussed crystals, and also describes how refraction at the Perspex-steel interface is dealt with for angled beam probes.

C2 Response of a flat-bottomed hole (FBH) reference reflector

It is useful to be able to calculate the signal which this beam would give rise to from a circular disc reflector lying at normal incidence on the beam axis. Such a signal can be used as a reference standard for comparing with the signals from rough defects. One advantage of the beam expression equation (C2) (and indeed the reason why it was devised) is that it can be integrated analytically to a close approximation to give a closed form expression for the signal from simple reference reflectors.

Allowing for the reciprocity of transmission and reception, the on-axis signal in pulse-echo from a smooth disc reflector of radius a at range z is the integral of [(C2) squared times the obliquity factor] over the area of the reflector:

$$\text{FBH Signal} \propto 2\pi \int_0^a \rho\,\psi^2(z,\rho)(\mathbf{e_s}\cdot\mathbf{n})\,d\rho \tag{C3}$$

To a sufficient approximation the range $R = \sqrt{(z^2 + \rho^2)}$ can be replaced by $z + \rho^2/(2z)$ and the obliquity factor is $1 - \rho^2/(2z^2)$. The 'R' in B can be replaced by z to give B_z and we thus obtain

$$\text{FBH Signal} \propto 2\pi \left(\frac{\pi N}{zB_z^2}\right)^2 e^{2ikz} \int_0^a \rho\left(1 - \frac{\rho^2}{2z^2}\right)(1 - 2A_\rho + A_\rho^2)\exp\left(-2A_\rho + \frac{ik\rho^2}{z}\right) d\rho. \quad (C4)$$

This is a sum over integrals of the form:

$$I_n = \int_0^a \rho^n \exp(-q\rho^2)\, d\rho \quad (C5)$$

for odd powers of ρ. The values required are

$$I_1 = \frac{1}{2q}[1 - \exp(-qa^2)]$$

$$I_3 = \frac{1}{2q^2}[1 - (qa^2 + 1)\exp(-qa^2)]$$

$$I_5 = \frac{1}{2q^3}[2 - (q^2a^4 + 2qa^2 + 2)\exp(-qa^2)]$$

$$I_7 = \frac{1}{2q^4}[6 - (q^3a^6 + 3q^2a^4 + 6qa^2 + 6)\exp(-qa^2)]$$

Appendix D: Shadowing of one facet by another on rough surfaces

At normal incidence on the defect, all of its surface will be illuminated by sound, unless there are re-entrant parts like tiny caves in the surface. However with increasingly oblique incidence there will be the increasing likelihood of some parts of the surface being screened from the incident beam by other parts, and these dark areas will not be able to scatter sound directly back to the probe. Therefore, the signal amplitude will be reduced, depending on the fraction of the surface in shadow. This appendix describes the approximate methods used to quantify this loss in signal. Shadowing is succinctly reviewed by Jill Ogilvy in reference 3.

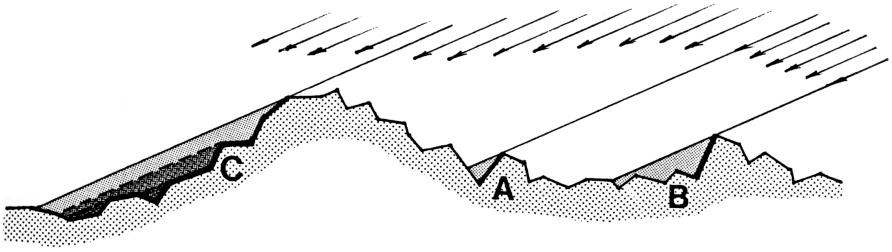

Figure D2 : Shadowing on a randomly facetted surface.

As we might expect, the matter is quite complicated, and gets more complicated as the angle of incident approaches grazing. Figure D1 shows in two dimensions the sorts of shadowing which will occur. At A we have the simplest case where one facet, which itself is in shadow, casts a shadow over part of the adjacent facet. At B a facet is sufficiently large and high that it throws several neighbouring facets into shadow. At C the surface as a whole has a hill-like geography such that one whole side of the hill is in shadow. In this case any particular facet can be in the shadows of two or even more facets. We might call this "deep shadow".

As noted in the Section 2 of the report, in principle shadowing could the calculated numerically once the triangular facet structure of a surface is defined. Rays would have to be traced from all the edges of the facets back to the probe and a rather involved algorithm used to determine the projections of one facet's edges on all other facets[16]. Facets or parts of facets not shadowed by any other facets could thereby be identified, and only these specific regions would contribute to the received signal. It will be clear, however, that such a calculation would be very involved in three-dimensions and would require a great deal of computer memory. Even then, it would not include the effect of diffraction which is to blur over the edges to the shadows.

In the face of this great complexity, a much simpler approach is required. Note at A in Figure D1 there can be no shadowing until there is at least one facet at which the local angle of incidence exceeds 90°. This is readily detected in the calculation by the dot product $\mathbf{n} \cdot .\mathbf{b}$ being negative. As, stated in Appendix B the reflection from that facet is set equal to zero, since it is not possible for the facet to be illuminated from its underside. In the program

[16] Today computer graphics program have fast in-built algorithms for hidden line removal and photo-realistic rendering of images of 3D objects based on ray-tracing.

the number of facets with $\mathbf{n} \cdot \mathbf{b} \leq 0$ is counted. A signal ψ_{int} is calculated by adding the non-zero contributions from all facets with $\mathbf{n} \cdot \mathbf{b} > 0$, and the resulting pulse is attenuated by an average geometrical shadowing factor which allows for the area of surface which is obscured by other parts. This shadowing factor is discussed below. Note that this approach makes most use of the information we can readily gain on *which* parts of the surface are in shadow. Discounting the under-illuminated facets gives some way of recognising and allowing for hills in the geography of the surface, and their exclusion can affect the pulse shape. An average shadowing factor cannot alter the pulse shape.

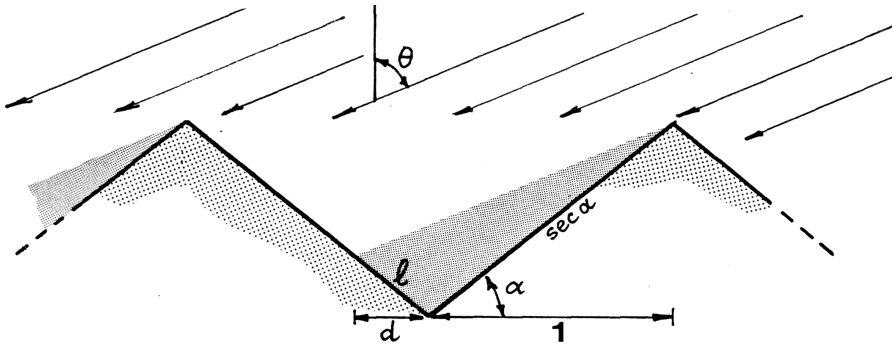

'Sine rule" : $\frac{\ell}{\sin(\alpha+\theta-\pi/2)} = \frac{\sec\alpha}{\sin(\alpha-\theta+\pi/2)}$

so $d = \ell\cos\alpha = -\cos(\alpha+\theta)/\cos(\alpha-\theta)$.

Figure D2 : Derivation of geometrical shadowing function for a simple 'dog tooth' surface.

Shadowing factors in the geometrical optics limit have been derived and discussed in the literature, as reviewed by Ogilvy (ref. 3). They are all quite complicated expressions, so before stating the expression used in the scattering program, we briefly examine a very simple illustrative two dimensional case. One of the simplest faceted surfaces is a regular dog-tooth of triangles as shown in Figure D2. Let the slope of each facet be α and suppose a beam is incident at angle θ from the normal to the mean plane of the surface. In this model α is also the angle corresponding to the root mean square slope. All the surface remains in full illumination until the beam grazes the right hand facets at $\theta = 90° - \alpha$. Then the right hand facet becomes dark, and with increasing angle of incidence it casts a lengthening shadow up the left facet. Following the short calculation in Figure D2, the illuminated fraction of the projected length of the surface is found to be

$$S_1 = \tfrac{1}{2}\left\{1 + \frac{\cos(\alpha+\theta)}{\cos(\alpha-\theta)}\right\}.$$

Figure D3 is a family of graphs of this expression as a function of θ for surfaces with a slope α from 10° to 80°.

Now in the scattering program the signal from the right hand facet will already have been set to zero once it tried to be illuminated from its underside. Consequently, if we were to multiply the signal as calculated, ψ_{int}, by S_1, we would be over compensating for shadowing, through twice deleting the contribution from the right hand facet. The shadowing factor we require should apply only to that fraction of surface which is capable of contributing a non-zero signal, which is $(1 - F_s)$ (see Eq 1).. In this simple example it is obviously $\frac{1}{2}$ so in this

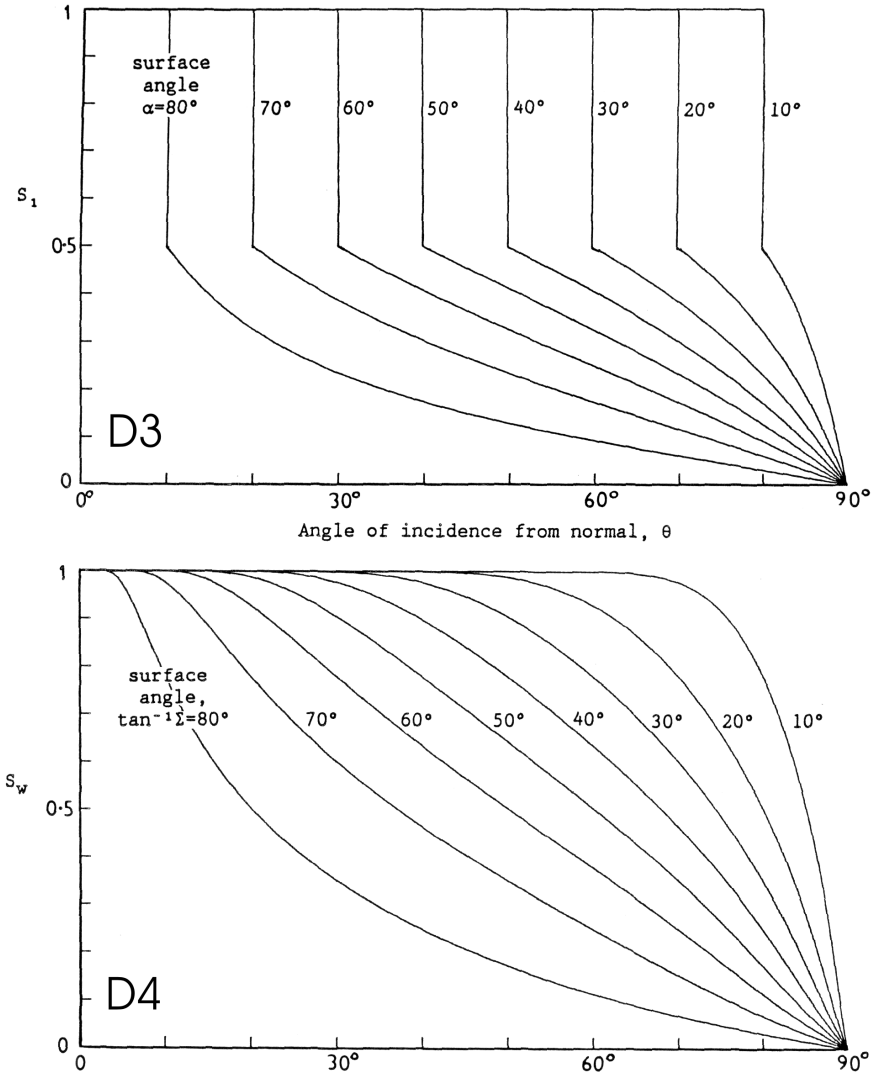

Figures D3 and D4 : D3 shows shadowing function S_1 for 'dog tooth' surface of Figure D2. D4 shows shadowing function S_w for a Gaussian surface after Wagner (ref. 13). Σ is the rms slope.

case the shadowing factor applied to the calculated signal for $\theta > 90° - \alpha$ would be $2S_1$, which has a maximum value of unity when $\theta = 90° - \alpha$.

This argument can be extended to more realistic surfaces using published expressions for geometrical shadowing functions. Clearly the main prediction of a more realistic model will be to smooth out the discontinuity where the rms slope $\alpha = 90° - \theta$. The function we use was devised by R. Wagner (ref. 13), and expresses the average fraction of the projected area of a Gaussian random surface which is in shadow, irrespective of the cause of this shadow. It therefore includes parts of the surface which would be illuminated from the underside. Wagner's function is equation A29 in the appendix to his paper and is given in Table D1

Figure D4 shows the equivalent family of curves for this expression to Figure D3. In the program the rms slope E is calculated directly from the co-ordinates of the triangle vertices as described in Appendix E2.

	S_w =	$\frac{1}{B}[2 - \mathrm{erfc}(v)]\,[1 - \exp(-B/2)]$
where	v =	$\frac{1}{\sqrt{2}.\Sigma \tan\theta}$
	Σ =	rms slope $= \sqrt{2}\,.\,\sigma/T$ for a Gaussian rough surface with standard derivation of heights σ and correlation function $\exp[-\tau^2/T^2]$.
	θ =	angle of incidence from normal.
	B =	$\frac{\exp(-9v^2/8)}{\sqrt{3}.\pi v} + \frac{\exp(-v^2)}{\sqrt{\pi}.v} + \mathrm{erfc}(v)$
	erfc	is the complementary error function.

Table D1. Wagner's shadowing function.

Recalling that F_s is the fraction of triangular facets which do not contribute to the calculated signal, the signal value output from the program is obtained from the intermediate value ψ_{int} by multiplying by $S_w/(1-F_s)$. Should $S_w/(1-F_s)$ ever exceed unity, its value would be set equal to 1, so that shadowing cannot seem to increase the signal!

Appendix E: Some statistical properties of randomly rough facetted surfaces

In the course of the scattering program the roughness of the surface is calculated in terms of the rms height relative to a reference plane. In addition the rms slope of the surface is needed to calculate the average effect of shadowing, as Appendix D describes. This appendix gives the methods for evaluation of these statistics from the co-ordinates of the facets' corners.

El Root mean square height deviation of a facetted surface

The defect is defined by the co-ordinates of its vertices in the (x, y, x) frame of Figure 1. The method used to calculate the rms height deviation from the (x, y) reference plane is to evaluate an analytical expression for the variance (equal to the rms height squared) of each triangle, and to add the variances numerically over all the triangles with appropriate weightings.

The definition of variance is:-

$$\int_{-\infty}^{+\infty} (z - z_m)^2 \, P(z) \, dz \qquad (e1)$$

where z is the height, z_m the mean height and $P(z)$ the probability distribution function of surface heights. In our case we take z to be zero. Strictly this means that the mean plane of the surface corresponds with the reference surface. Whether or not this is true to an acceptable approximation depends on how the data file of surface height values is generated, following the experimental or numerical methods described in Section 5. For the present we assume that the mean plane and the (x, y) reference plane do coincide; if they do not, then the method used for calculating the rms height deviation will give an overestimate.

The calculation of variance as the sum of contributions from individual triangles follows from the interpretation of $P(z).dz$ in the definition of variance, equation (el). Imagine a thin slice, δz wide, taken across the rough surface, parallel to the (x, y) reference plane at height z. Triangles which reach to a height greater than z will be cut by a narrow stripe over heights z to $z + \delta z$, and we imagine these stripes to be projected onto the (x, y) plane. Then $P(z).dz$ is simply the sum over all triangles of the projected areas of stripes, expressed as a fraction of the total projected area of the defect.

The problem therefore reduces to evaluating the double integral of $z^2(x, y)$ over z and over the stripes in the (x, y) plane. Suppose one typical triangular facet has vertices whose position vectors are $\mathbf{P_1}$, $\mathbf{P_2}$, $\mathbf{P_3}$, where P_1 is placed for calculational convenience over the origin O. A point P in the plane of the triangle satisfies $\mathbf{P_1} \cdot \mathbf{P_2} \times \mathbf{P_3} = \mathbf{0}$, and from this relation the height z at a general point (x, y) can be found. This defines the stripes and allows the integration over z to be performed. The projection of the triangle onto the (x, y) plane has vertices O, P_1', P_2'. The limits of integration over the projected triangle are the lines L_1, L_2, L_3, where L_1, is the side joining P_2 to the origin, and so forth as in Figure B1. The integration over x and y can be done by dividing the projected triangle into two sub-triangles,

rather as in Figure B1. The result for the integral of z^2 is:

$$\frac{1}{12} f(P_{1z},\, P_{2z},\, P_{3z}).\Delta' \qquad (e2)$$

$$\text{where } f(a,b,c) = a^2 + b^2 + c^2 + ab + ac + bc.$$

and the subscripts on P imply the obvious Cartesian components. Δ' is the projected area of the triangle, which appears in the maths in the form $\frac{1}{2}[P_{2x}P_{3y} - P_{3x}P_{2y}]$, $P_{1x,y}$ being taken as zero. Hence the required variance of surface height deviations for the whole defect is the sum over triangles of equation (e2), divided by the projected area of the defect. In fact

$$\frac{1}{6} f(P_{1z},\, P_{2z},\, P_{3z}) \qquad (e3)$$

is the variance of height, z, for the one triangle.

E2 Average slopes of the facets

The average"angle of the facets is a statistical measure of the quality of the surface morphology and also the rms slope is required for the calculation of shadowing. The program evaluates three quantities set out below.

E2.1 RMS facet tilt angles

In the course of the co-ordinate transformation of Appendix A the program obtains the unit normal to each facet, $\mathbf{e_w}$, in the (x, y, z) co-ordinate system of the defect. The z component of this is the cosine of the angle by which that facet is tilted with respect to the reference plane (x, y). Denoting the projected area of the jth facet onto (x, y) by Δ'_j, we obtain the rms facet tilt angle from:-

$$\left\{ \frac{\sum_j^N \Delta'_j \left[\arccos(\mathbf{e_w} \cdot \mathbf{e_z})_j\right]^2}{\sum_j^N \Delta'_j} \right\}^{\frac{1}{2}} \qquad (e4)$$

for the N triangles in all.

E2.2 Surface anisotropy

Each facet is a plane with form

$$z = ax + by + c. \qquad (e5)$$

The coefficients a and b are the gradients of the facet in the x and y directions respectively. For each triangle a, b and c are calculated. They are given by the solution of the three simultaneous linear equations obtained by evaluating (e5) at the three vertices of the triangle. The ratio:

$$\left\{ \frac{\sum_j^N \Delta'_j\, b_j^2}{\sum_j^N \Delta'_j\, a_j^2} \right\}^{\frac{1}{2}} \qquad (e6)$$

is the ratio of the rms slopes in the x and y directions. It gives a measure of the surface anisotropy for cases when the surface is 'stretched' in either the x or y directions, as is possible with the random surfaces generators described in this report.

Note in passing that $\sqrt{a^2+b^2}$ is the maximum gradient of the facet and that

$$\tan^{-1}\sqrt{(a^2+b^2)} \;=\; \cos^{-1}(\mathbf{e_w}\cdot\mathbf{e_z}). \qquad (e7)$$

E2.3 RMS surface slope as seen from the ultrasonic beam

For shadowing calculations we wish to know the rms slope as seen by the ultrasonic beam. If the beam is incident in azimuth ϕ (Figure I) with respect to the (x, y, z) co-ordinate system, the slope of the jth facet in this direction is

$$a_j \cos\phi + b_j \sin\phi. \qquad (e8)$$

For an isotropic surface averages of this quantity will be equal to the equivalent averages of a_j and of b_j. However, the program acknowledges the possibility of surface anisotropy and calculates

$$\cos^2\phi \sum_j^N \Delta'_j\, a_j^2 \;+\; \sin^2\phi \sum_j^N \Delta'_j\, b_j^2 \;+\; 2\cos\phi\sin\phi \sum_j^N \Delta'_j a_j b_j \qquad (e9)$$

which leads directly to the required rms slope for use in Wagner's expression for shadowing, Appendix D.

Appendix F: Reliability of algebra and software

It is worth recording some of the steps taken to ensure that the algebra and software of the current program are accurate. The algebra of the co-ordinate transformations, of the Kirchhoff wave scattering, surface roughness statistics, *etc.* were worked out and checked by hand by the author. Special cases where the answer is obvious were also used to check the answer and some of these are noted in the relevant Appendices. In addition the principal expressions in Appendixes B and E were derived on a computer using the LISP algebraic manipulation package REDUCE. As a further check, Dr. Chapman re-derived the formulae and checked the software coding when he translated the program from BASIC to FORTRAN.

One important check has been to compare the signal response for a flat, smooth, approximately circular defect made up of triangular tiles with the response evaluated from the analytical expression for a perfectly circular defect under the same conditions. The difference in amplitude between these is due mainly to the small difference in area provided we go to sufficient range that the beam illuminates circle and polygon uniformly. Unless this is done, the shape difference causes a genuine difference in signal. Here is an example for a 4 MHz, 10 mm diameter shear wave probe at 250 mm range:

Perfect circle 2 m diameter:	Signal	$5 \cdot 28$ dB
Polygonal defect about 2 mm diam:	c.w. calculation	$3 \cdot 20$ dB
	pulse calcn	$3 \cdot 18$ dB
Mean difference in amplitude		$2 \cdot 09$ dB
Ratios of area circle/polygon	$= 12 \cdot 57/9 \cdot 86$	$= (1.13)^2$
Difference in dB due to difference in area		$2 \cdot 11$ dB
Hence genuine discrepancy between analytical result and triangle calculation		$0 \cdot 02$ dB
Check : signal from circle $0 \cdot 02$ mm diam. according to analytical expression		$3 \cdot 20$ dB

The discrepancy is very small. Further confirmation comes from the fact that only similarly small discrepancies occur whatever the pattern of triangles used to 'pave' the almost circular defect.